

Investigating Dual AGN/SMBH: A Study of Dual AGN MRK 739 in High Energy Astrophysics

THESIS

Submitted in partial fulfillment

of the requirements for the Master's degree

Gaurav Ganpat Gawade

Under the guidance of

Dr. Manojendu Choudhury



Department of Physics

St. Xavier's College (Autonomous), Mumbai

2024

THESIS SUBMITTED TO ST. XAVIER'S COLLEGE, MUMBAI
FOR THE MASTER'S DEGREE IN PHYSICS

Name of the student: Gaurav Ganpat Gawade
UID no.: 229118
Name of the guide: Dr. Manojendu Choudhury
Designation and affiliation of
guide: Assistant Professor, Department of Physics,
St. Xavier's College (Autonomous), Mumbai, India
Dissertation title: "Investigating Dual AGN/SMBH: A Study of Dual AGN
MRK739 in HIGH ENERGY ASTROPHYSICS"
Submission date: 15-03-2024

Signature of student: _____

Signature of guide: _____

ACCEPTANCE OF SUBMISSION

Name of the assigned
departmental mentor: Dr. Katherine Rawlins
Designation of mentor: Assistant Professor, St. Xavier's College(Autonomous), Mumbai

Signature of mentor (with date): _____

CERTIFICATION OF SUCCESSFUL COMPLETION OF THESIS AND VIVA

Signature of certifying authority: _____ Date: _____
Name and designation of certifying authority: _____

UNDERTAKING BY THE STUDENT

I declare that the work embodied in the thesis entitled "Investigating Dual AGN/SMBH: A Study of Dual AGN Mrk 739 in HIGH ENERGY ASTROPHYSICS" represents my own contribution to the research carried out under the guidance of Dr. Manojendu Choudhury from St. Xavier's College (Autonomous), Mumbai, India.

The work presented in this thesis has not been submitted for the award of any other degree to this or any other institute. References to other research studies have been duly acknowledged and included in the bibliography.

The thesis has been checked for plagiarism using the software Turnitin, and the soft copy of the report is being submitted along with this thesis.

Date 15-03-2024

Name and signature of student

Gaurav Ganpat Gawade

CERTIFICATE FROM GUIDE

I certify that the thesis entitled **Investigating Dual AGN/SMBH: A Study of Dual AGN Mrk 739 in HIGH ENERGY ASTROPHYSICS** submitted by **Gaurav Ganpat Gawade** for the award of Master's degree, embodies original work done by him/her under my guidance.

This work has not been submitted to this or any other institute for the award of any other degree.

Date _____

Name and signature of guide _____

Designation and affiliation **Assistant Professor,**

St. Xavier's College (Autonomous),

Mumbai, India

Acknowledgements

I extend my sincerest gratitude to Dr. Manojendu Choudhury, whose invaluable guidance, unwavering support, and profound insights have been instrumental throughout the entirety of this research endeavor. His guidance has not only shaped the direction but also enhanced the quality of this thesis, profoundly influencing its scholarly contributions.

I would also like to express my heartfelt appreciation to Dr. Katherine Rawlins, the departmental mentor, for her constructive feedback, expert advice, and unwavering encouragement at various stages of this study. Additionally, I extend my gratitude to Dr. Amruta Sadhu, whose expertise in Theoretical Physics proved indispensable in elucidating complex theoretical aspects crucial to gaining deeper insights into the functioning of Supermassive Black Hole Binary systems. Their contributions have significantly enriched the content and rigor of this research.

Special acknowledgment is owed to Mr. Chintan Patel and Ms. Simran Ghag, my seniors for their guidance in understanding the fundamentals of X-ray spectral analysis. I am equally grateful to Mr. Narendra Bhatkar and Ms. Krishna Bulchandani, my classmates, for their invaluable assistance in troubleshooting technological challenges encountered during the course of this thesis.

Furthermore, I extend my gratitude to Prof. Richard Mushotzky, Prof. Mike Koss, Prof. Ryosuke Uematsu, and Dr. Scott Noble for their generous provision of email support, aiding in the resolution of queries pertaining to their esteemed publications. Their contributions have been immensely beneficial in advancing the scholarly discourse within this research domain.

Special recognition is also extended to the CXO Support team for their invaluable assistance in addressing software-related issues pertaining to the CIAO software, an essential tool for Chandra X-ray Data Analysis.

I am deeply indebted to St. Xavier's College (Autonomous), Mumbai, for providing the necessary resources and facilities crucial to the successful completion of this thesis. Their unwavering support has been pivotal in facilitating the execution of this scholarly endeavor.

Heartfelt appreciation is extended to my family for their unwavering love, encouragement, and

understanding throughout this academic pursuit. Their steadfast belief in my abilities has served as a constant source of strength and motivation, driving me towards academic excellence.

Lastly, I extend my sincerest gratitude to all the participants who generously contributed their time, insights, and experiences to this research endeavor. Without their invaluable contributions, this research would not have been possible, underscoring the collaborative nature inherent within the scholarly pursuit of knowledge.

This thesis stands as a testament to the collective efforts, support, and guidance provided by the aforementioned individuals and institutions, for which I am profoundly grateful.

Gaurav Ganpat Gawade

Abstract

Active Galactic Nuclei (AGN) serve as the dynamic powerhouses at the heart of galaxies, fundamentally driven by supermassive black holes (SMBHs). While it is established that each galaxy contains at least one AGN/SMBH, recent observations suggest the intriguing possibility of galaxies hosting dual AGN/SMBH at their cores. Termed as dual AGN, these systems emerge from the collision or merger of two significantly large galaxies. This interaction leads to the formation of dual AGN, which, under certain conditions, may evolve into more compact configurations known as binary AGN.

In this thesis, we delve into the investigation of dual AGN and their detection methodologies within the high-energy astrophysical domain, emphasizing image and spectral analysis. The initial phase of our study leverages image analysis to identify candidates of dual AGN, laying the groundwork for a subsequent, more in-depth exploration of their characteristics through spectral analysis. Our research primarily centers on the dual AGN system Mrk 739 (Markarian 739), aiming to enrich our understanding of its image and spectral properties. By harnessing data from a suite of observatories, including Swift, NuSTAR, XMM-Newton, and Chandra, we have compiled a comprehensive dataset to analyze the source extensively. This multifaceted approach not only enhances our knowledge of Mrk 739 but also enables a comparative assessment of the capabilities and contributions of these X-ray observatories to the field.

Throughout this research, we conducted a comparative analysis of various characteristics pertaining to the source and estimated the projected nuclear separation of the dual AGN Mrk 739 to be approximately 3.6 kpc. Moreover, our study extends beyond Mrk 739 to include discussions on additional dual AGN systems and candidates, notably highlighting NGC 6240, a well-documented binary AGN.

Overall, this systematic examination of the dual AGN Mrk 739 enriches our understanding of dual AGN phenomena. By applying the methodologies developed here, we have the potential to uncover more dual AGN sources. Advancing this line of inquiry in the future promises to make significant contributions to the broader domain of galactic dynamics.

Contents

| | | |
|-------|--|----|
| 1.1 | Overview of Active Galactic Nuclei (AGN) | 19 |
| 1.2 | Terminologies Summary | 20 |
| 1.3 | Multiwavelength Study of Dual AGN | 21 |
| 1.3.1 | Radio Observations | 21 |
| 1.3.2 | Optical and Infrared Observations | 22 |
| 1.3.3 | X-ray Observations | 22 |
| 1.3.4 | Gamma-Ray Observations | 22 |
| 1.3.5 | Multimessenger Astronomy: Gravitational Waves | 22 |
| 1.4 | Binary AGN | 23 |
| 1.4.1 | Keplerian Motion in Binary Systems | 23 |
| 1.4.2 | Observational Signatures of Binary AGN | 24 |
| 1.4.3 | Evolution and Coalescence of Binary AGN | 24 |
| 2.1 | SMBH Dynamics, Galaxy Evolution, and Dual AGN Observations | 26 |
| 2.2 | Supermassive Black Hole Binary Dynamics | 26 |
| 2.2.1 | Theoretical Frameworks | 27 |
| 2.2.2 | Stellar and SMBH Interactions | 27 |
| 2.2.3 | Gas Dynamics | 27 |
| 2.2.4 | Observational Challenges | 27 |
| 2.3 | Future Perspective | 27 |
| 3.1 | Neil Gehrels Swift Observatory | 30 |
| 3.1.1 | Swift/XRT (X-ray Telescope) | 30 |
| 3.1.2 | Swift/BAT (Burst Alert Telescope) | 31 |
| 3.1.3 | Swift/UVOT (Ultra-Violet/Optical Telescope) | 32 |
| 3.2 | NuSTAR | 33 |
| 3.3 | XMM-Newton | 34 |
| 3.4 | Chandra | 35 |
| 4.1 | Building and Installing HEASoft Software | 36 |
| 4.2 | Setting Up CALDB Environment | 38 |

| | | |
|--------|--|----|
| 4.3 | Data Reduction and Data Extraction | 39 |
| 4.4 | Swift/XRT | 40 |
| 4.4.1 | Creating Region Files | 40 |
| 4.4.2 | ARF and RMF Creation | 42 |
| 4.5 | SWIFT/BAT | 43 |
| 4.6 | XMM-Newton | 44 |
| 4.6.1 | SAS Installation | 44 |
| 4.6.2 | Data Preparation and Calibration | 44 |
| 4.6.3 | Generating Cleaned Event Lists | 45 |
| 4.6.4 | Image and Spectral Analysis | 45 |
| 4.7 | NuSTAR Data Reduction and Analysis | 46 |
| 4.8 | Chandra | 50 |
| 4.8.1 | CIAO Installation | 50 |
| 4.8.2 | Data Reduction and Analysis with CIAO | 50 |
| 4.9 | XSPEC Analysis | 52 |
| 4.10 | Understanding the Spectrum | 53 |
| 4.11 | Calculating the Nuclear Separation of the Dual AGN | 54 |
| 4.11.1 | Coordinate Conversion | 54 |
| 4.12 | Calculating Angular Separation | 54 |
| 4.12.1 | Using Pythagorean Theorem | 54 |
| 4.12.2 | Using the Spherical Law of Cosines | 55 |
| 4.12.3 | Conversion to Physical Units | 55 |
| 4.12.4 | Python Code for Calculating Nuclear Separation of dual AGN | 56 |
| 4.13 | RA and DEC Observations | 58 |
| 5.1 | Projected Nuclear Separation | 68 |
| 5.2 | SWIFT/XRT Spectra of Mrk 739 | 69 |
| 5.3 | SWIFT/BAT Spectra of Mrk739 | 73 |
| 5.4 | NuSTAR Spectra of Mrk 739 | 75 |
| 5.5 | XMM-Newton Spectra of Mrk 739 | 78 |
| 5.6 | Chandra/ACIS-S Observation of Mrk 739 | 80 |

| | |
|----------------------------|-----------|
| 6.1 Conclusion | 87 |
| 6.2 Future Scope | 87 |
| | |
| Appendix-A | 88 |
| | |
| Appendix-B | 91 |
| | |
| References | 93 |

List of Figures

| | | |
|----|---|----|
| 1 | Artist's impression of an Active Galactic Nucleus, illustrating the central supermassive black hole surrounded by an accretion disk and a dusty torus, with jets emanating perpendicular to the disk. Credits: ESA/NASA, the AVO project, and Paolo Padovani. | 20 |
| 2 | Stages of AGN/SMBH/BH-BH Merging http://arxiv.org/abs/1502.05720 | 25 |
| 3 | Schematic Diagram of Swift Observatory showcasing its main 3 telescopes, namely XRT, UVOT, and BAT. | 30 |
| 4 | Schematic Diagram of XRT.(Burrows et al., 2005) | 31 |
| 5 | Schematic Diagram of BAT.(Barthelmy et al., 2005) | 31 |
| 6 | UVOT Layout. (Roming et al., 2005) | 32 |
| 7 | Schematic Diagram of NuSTAR X-ray Observatory. Credits: NASA/HEASARC Harrison et al., 2013 | 33 |
| 8 | Schematic Diagram of XMM-Newton X-ray Observatory. Credits - ESA/XMM-Newton | 34 |
| 9 | The Chandra X-ray Observatory. Image Courtesy - NASA/Chandra(<i>Chandra Proposers' Observatory Guide</i> , 2021) | 35 |
| 10 | Selecting regions in DS9 using SWIFT/XRT Data | 41 |
| 11 | NuSTAR Data Structure Flowchart. Credits - HEASARC | 46 |
| 12 | DS9 Region Selection Process using Nustar Image | 47 |
| 13 | DS9 Region Selection Process with Chandra image | 51 |

| | | |
|----|--|----|
| 14 | Example of an X-ray spectrum fitted with an absorbed power-law model. Key features include the continuum shape determined by the power-law and absorption edges modeled by tbabs. | 53 |
| 15 | Mrk739 Eastern Component | 58 |
| 16 | Mrk739 Western Component | 58 |
| 17 | Mrk 739 East (left) and Mrk 739 West (right) as resolved by Chandra's High-Resolution Camera on the ACIS/S. The contours illustrate intensity levels across the RA and DEC grid. | 59 |
| 18 | Comparison of SWIFT/XRT and Chandra ACIS/S images of Mrk 739. | 59 |
| 19 | XMM-Newton/OM Image of Mrk739. ¹ | 60 |
| 20 | Grey-scale image is the 1.49 GHz VLA data, while the contours are the 4.86 GHz data convolved to 1.49 GHz beam. White ×'s indicate the Chandra hard X-ray positions | 60 |
| 21 | The Chandra ACIS/S image of the dual AGN, Mrk 266, is depicted alongside a standard RA DEC coordinate grid. Cross marks denote the predicted positions of the AGN, coinciding with regions exhibiting the highest intensity of X-ray emission. | 61 |
| 22 | The Chandra ACIS/S image of the candidate dual AGN, J125929.9+275723. | 62 |
| 23 | The Chandra ACIS/S image of the candidate dual Active Galactic Nuclei (AGN), Mrk 463, is presented with contours indicating X-ray intensity levels. Cross marks overlay the image, indicating the predicted positions of the AGN, which correspond to regions of highest X-ray emission intensity. | 63 |
| 24 | The Chandra ACIS/S image of the candidate dual Active Galactic Nuclei (AGN), NGC6240 | 64 |

| | | |
|----|--|----|
| 25 | The Chandra ACIS/S image displays the dual AGN, NGC 7674, situated in the southern region of the image. Additionally, a potential companion AGN is observed in the northern portion of the image.) | 65 |
| 26 | The Chandra ACIS/S image of the candidate dual AGN, J131517.3+442425 . . . | 66 |
| 27 | The Chandra ACIS/S image of the candidate dual AGN, 4211. | 67 |
| 28 | SWIFT/XRT Obs ID: 00037134001. Observed on date 2007-07-20 with XRT exposure of $\approx 4\text{ks}$ | 69 |
| 29 | SWIFT/XRT Obs ID: 00037134002. Observed on date 2015-10-14 with XRT exposure of $\approx 8\text{ks}$ | 70 |
| 30 | SWIFT/XRT Obs ID: 00081813001. Observed on date 2017-03-16 with XRT exposure of $\approx 2\text{ks}$ | 71 |
| 31 | SWIFT/BAT Spectrum of Obs ID: 00037134002. Observed on date 2008-07-11 with BAT exposure of $\approx 8\text{ks}$ | 73 |
| 32 | SWIFT/BAT Lightcurve of Obs ID: 00037134002. Observed on date 2008-07-11 with BAT exposure of $\approx 8\text{ks}$ | 74 |
| 33 | NuSTAR/FPMA Spectrum Obs ID: 60260008002. Observed on date 2017-03-16 with the exposure of $\approx 18\text{ks}$ | 75 |
| 34 | Simultaneous Spectra of NuSTAR's FPMA and FPMB Modes. Obs ID: 60260008002. Observed on date 2017-03-16 with the exposure of $\approx 18\text{ks}$ | 76 |
| 35 | XMM-Newton/PN Spectrum Obs ID: 0601780401. Observed on date 2009-06-14 with the exposure of $\approx 12\text{ks}$ | 78 |
| 36 | Chandra/ACIS-S Spectrum of Mrk 739W, Obs ID: 12863. Observed on date 2011-04-22 with the exposure of $\approx 13\text{ks}$ | 80 |

| | | |
|----|--|----|
| 37 | Chandra/ACIS-S Spectrum of Mrk 739W, Obs ID: 12863. Observed on date 2011-04-22 with the exposure of $\approx 13\text{ks}$ | 81 |
| 38 | Chandra/ACIS-S Spectrum of Mrk 739W, Obs ID: 12863. Observed on date 2011-04-22 with the exposure of $\approx 13\text{ks}$ | 82 |
| 39 | Simultaneous Folded Spectrum of Mrk739E, Mrk739W and (Mrk739E+Mrk739W) | 84 |
| 40 | Simultaneous Unfolded Spectrum of Mrk739E, Mrk739W and (Mrk739E+Mrk739W) | 85 |
| 41 | Simultaneous Unfolded Spectrum of Mrk739E, Mrk739W and (Mrk739E+Mrk739W) | 86 |
| 42 | NuSTAR Image of Mrk 739 | 88 |
| 43 | XMM-Newton/EPIC X-ray Image of Mrk 739 | 89 |
| 44 | Comparison of Soft and Hard X-ray Images of Mrk 739 | 90 |
| 46 | Spectrum of NGC 6240 Composite (North + South) | 91 |
| 47 | Spectra of Mrk 463 (East and West Components) | 92 |
| 48 | Spectrum of Mrk 463 Composite (East + West) | 92 |

List of Tables

| | | |
|---|---|----|
| 1 | Key AGN Terminologies | 21 |
| 2 | Overview of Notable Astronomical Surveys | 29 |
| 3 | RA and DEC Observations for Mrk739 Components | 58 |
| 4 | Observational Data Summary | 68 |
| 5 | Observation IDs and Spectral Parameters | 72 |
| 6 | Spectral Parameters of 60260008002 | 77 |
| 7 | Spectral Parameters of 601780401 | 79 |
| 8 | Spectral Parameters of Mrk739E, Mrk739W, and Combined | 83 |

List of Abbreviations

2MASS Two Micron All Sky Survey

AGN Active Galactic Nucleus

ARF Ancillary Response Files

Athena Advanced Telescope for High ENergy Astrophysics

AXIS Advanced X-ray Imaging Satellite

BH Black Hole

CALDB Calibration Database

CANDELS Cosmic Assembly Near-infrared Deep Extragalactic Legacy Survey

CDFS Chandra Deep Field South

Chandra/ACIS-S Chandra's Advanced CCD Imaging Spectrometer-S

CIAO Chandra Interactive Analysis of Observations

cl_evt Cleaned Event File

CMB Cosmic Microwave Background

COSMOS COSMic evOlution Survey

CXC Chandra X-ray Center

DEC Declination

DES Dark Energy Survey

DPI Detector Plane Image File

EM Electromagnetic

EPIC European Photon Imaging Camera

ESA European Space Agency

ESO European Southern Observatory

eROSITA extended ROentgen Survey with an Imaging Telescope Array

FIR Far-Infrared

FITS Flexible Image Transport System

GAIA Global Astrometric Interferometer for Astrophysics

GOALS Great Observatories All-sky LIRG Survey

GRB Gamma Ray Burst

GRPPHA Group Pulse Height Analyzer

GW Gravitational Wave

HST Hubble Space Telescope

IFU Integral Field Unit

JWST James Webb Space Telescope

keV Kilo Electron Volt

LISA Laser Interferometer Space Antenna

LSST Large Synoptic Survey Telescope

MIRI Mid-Infrared Instrument

Mrk Markarian

NASA National Aeronautics and Space Administration

NGC New General Catalogue of Nebulae and Clusters of Stars

NIR Near-Infrared

NIRCam Near-Infrared Camera

NuSTAR Nuclear Spectroscopic Telescope Array

PC Mode Photon Counting Mode

PHA Pulse Height Analyzer

PI Pulse Invariant

PTA Pulsar Timing Array

RA Right Ascension

RMF Response Matrix Files

Sgr A* Sagittarius A*

SMBH Supermassive Black Hole

SMBHB Supermassive Black Hole Binary

SAO/DS9 Smithsonian Astrophysical Observatory's Deep Space 9

SDSS Sloan Digital Sky Survey

SKA Square Kilometre Array

subkpc Sub-Kilo Parsec

subpc Sub-Parsec

Swift/BAT Swift Observatory's Burst Alert Telescope

Swift/XRT Swift Observatory's X-ray Telescope

UGC Uppsala General Catalogue of Galaxies

uf_evt Unfiltered Event File

VLA Very Large Array

VLASS VLA Sky Survey

VLBI Very Long Baseline Interferometry

VODKA Varstrometry for Off-nucleus and Dual Subkiloparsec AGN

GOTHIC Graph-bOosTed iterated Hill Climbing

VISTA/4MOST Visible and Infrared Survey Telescope for Astronomy/4-metre Multi-Object Spectroscopic Telescope

WHT/WEAVE William Herschel Telescope/WHT Enhanced Area Velocity Explorer

WISE Wide-field Infrared Survey Explorer

WT Mode Windowed Timing Mode

XMM-Newton X-ray Multi-Mirror Mission - Newton

XMM-Newton/PN XMM-Newton's pn-CCD

XSPEC X-Ray Spectral Fitting Package

$\Delta\chi^2$ Delta-Chisquared

CHAPTER 1: INTRODUCTION

1.1 Overview of Active Galactic Nuclei (AGN)

Active Galactic Nuclei (AGN) represent some of the most energetic and enigmatic objects in the universe. These powerhouses are fueled by the accretion of material onto supermassive black holes (SMBHs) situated at the centers of galaxies. The gravitational potential energy of the accreted material is converted into radiation across the entire electromagnetic spectrum, rendering AGNs as some of the brightest objects in the cosmic landscape.

The concept of a SMBH, a region of space exhibiting such strong gravitational effects that nothing, not even particles and electromagnetic radiation such as light, can escape from it, underpins the nature of AGNs. SMBHs are characterized by their immense mass, typically ranging from millions to billions of times that of the Sun. The occurrence of SMBHs is not rare; in fact, it is believed that they reside at the core of most, if not all, massive galaxies. This prevalence suggests a significant role for SMBHs and, by extension, AGNs in the evolutionary pathways of galaxies.

The Milky Way itself harbors a SMBH at its center, known as Sgr A*. This particular SMBH offers a closer examination of these phenomena, providing invaluable insights into the dynamics and environment surrounding SMBHs. Though Sgr A* is considerably less luminous compared to typical AGNs as it is inactive, it serves as a prototype for understanding the physics of accretion and the mechanisms powering AGNs (Genzel et al., 2010).

AGNs are broadly classified based on their observable characteristics² into several categories including Seyfert galaxies, quasars, blazars, and radio galaxies. Seyfert galaxies display narrow emission lines indicative of high-velocity gas in the vicinity of the SMBH, while quasars, the most luminous AGNs, can outshine their entire host galaxy, being visible across vast cosmic distances. Blazars are noted for their jet emissions aligned towards the Earth, and radio galaxies emit significant radio waves, suggesting the presence of relativistic jets perpendicular to the plane of their accretion disks (Urry and Padovani, 1995).

²According to the widely accepted Unified Model of AGN, the classification of AGN is contingent upon the observer's viewing angle towards the object.

AGNs play a pivotal role in the context of galaxy evolution. The concept of AGN feedback—whereby the energy output from an AGN influences its host galaxy, regulating star formation and contributing to the heating of the intergalactic medium—highlights the importance of AGNs in shaping the properties of galaxies. Observations and simulations have shown that AGN feedback can lead to the suppression of star formation, thereby affecting the growth and evolution of galaxies (Fabian, 2012).

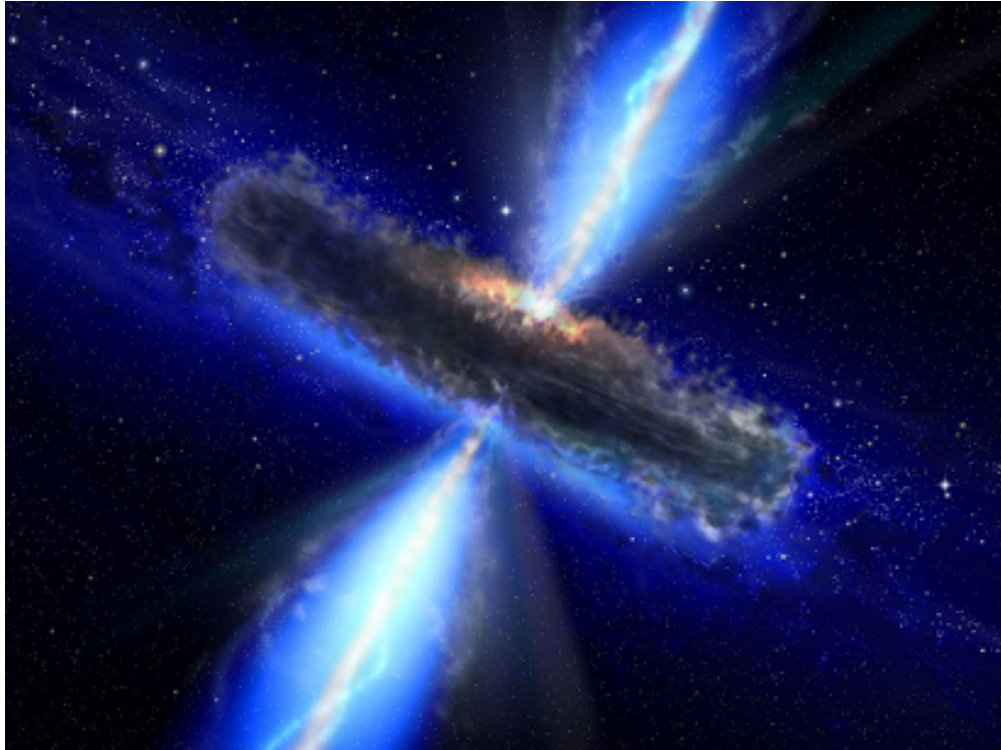


Figure 1: Artist’s impression of an Active Galactic Nucleus, illustrating the central supermassive black hole surrounded by an accretion disk and a dusty torus, with jets emanating perpendicular to the disk. Credits: ESA/NASA, the AVO project, and Paolo Padovani.

Research on AGN enhances our understanding of SMBHs and the fundamental mechanisms of galaxy evolution. Advances in telescopes and observational methods have greatly improved our knowledge of AGNs, providing deep insights into the high-energy-universe.

1.2 Terminologies Summary

This table summarizes key terminologies related to dual AGN studies.

Table 1: Key AGN Terminologies

| Term | Definition |
|-------------------------------|--|
| Dual AGN | Two AGN residing within the same galaxy, typically in late-stage galaxy mergers, identified through spatial and spectral diagnostics. Separations range from a few hundred parsecs to several kiloparsecs. |
| Binary AGN | A subset of dual AGN with two SMBHs gravitationally bound within a single nucleus, potential sources of GWs, indicating closer interaction than dual AGN. |
| Offset AGN | Dual AGN where one SMBH is active and the other is not. |
| Sub-kpc Dual AGN | Dual AGN with the nuclear separation of less than a kilo-parsec. |
| Sub-pc Dual AGN | Dual AGN with the nuclear separation of less than a parsec. |
| Merger Remnants & Coalescence | Galaxies that have recently merged, often hosting dual or binary AGNs. Coalescence is the final phase where SMBHs merge into a binary AGN. |

1.3 Multiwavelength Study of Dual AGN

The study of Dual AGN across multiple wavelengths is pivotal in understanding the multifaceted nature of these systems. Observations spanning from radio to gamma-ray frequencies provide a comprehensive view of the physical processes at play, offering insights into the accretion mechanisms, jet activity, and the impact of AGN on their host galaxies.

1.3.1 Radio Observations

Radio wavelengths are instrumental in probing the jet components of AGNs. Dual AGN systems often exhibit distinct radio signatures that can be attributed to jets or lobes ejected by the SMBHs. Very Long Baseline Interferometry (VLBI) allows for the resolution of these features at sub-parsec scales, enabling the study of jet morphology, orientation, and the dynamics of SMBH binaries (Burke-Spolaor et al., 2019). Furthermore, radio observations can reveal interactions between the jets and the interstellar medium, shedding light on the feedback mechanisms of AGNs.

1.3.2 Optical and Infrared Observations

Optical and infrared (IR) observations are critical for identifying and characterizing the stellar and dusty environments of Dual AGN. Spectroscopic surveys in the optical band can uncover the presence of dual AGNs through the detection of double-peaked emission lines, indicative of two distinct nuclear regions (Liu et al., 2010). Infrared observations, particularly with the advent of the James Webb Space Telescope (JWST), are poised to penetrate the dust-obscured regions around AGNs, allowing for the detection of dual AGN systems hidden from optical surveys.

1.3.3 X-ray Observations

X-ray astronomy has been at the forefront of dual AGN discovery and analysis. High-energy X-ray observations provide direct evidence of accretion onto SMBHs, with dual AGN systems often exhibiting two distinct, hard X-ray sources. Satellites such as Chandra, XMM-Newton, and NuSTAR offer the spatial resolution necessary to resolve closely spaced dual AGNs, while their spectral capabilities allow for the study of the accretion disk physics and the surrounding hot corona (M. Koss et al., 2012).

1.3.4 Gamma-Ray Observations

Although more challenging, gamma-ray observations of dual AGN offer a unique perspective on the highest energy processes occurring near SMBHs. Fermi-LAT and future gamma-ray telescopes aim to detect the signatures of particle acceleration and interaction within AGN jets, contributing to our understanding of the extreme physics governing these environments.

1.3.5 Multimessenger Astronomy: Gravitational Waves

Beyond electromagnetic observations, the emerging field of multi-messenger astronomy promises to revolutionize our understanding of dual AGN. PTA³ and future space-based gravitational wave observatories like LISA⁴ are expected to detect the gravitational waves emitted during the inspiral and merger of SMBH binaries (Burke-Spolaor et al., 2019). These observations will provide di-

³Pulsar Timing Array

⁴LISA (Laser Interferometer Space Antenna) is a space-based gravitational wave observatory designed to detect and study low-frequency gravitational waves.

rect measurements of SMBH masses, distances, and the dynamics of binary coalescence, offering unprecedented insights into the final stages of AGN evolution.

The multiwavelength study of dual AGN showcases astronomers' diverse tools and techniques, offering insights into the universe's energetic phenomena and enhancing our understanding of dual AGN systems' cosmic significance.

1.4 Binary AGN

Binary AGN represent a critical phase in the merger of galaxies hosting SMBHs. When two galaxies collide and merge, their central SMBHs can form a binary system, orbiting each other due to their mutual gravitational attraction. This section delves into the dynamics of binary AGN, including the Keplerian motion of binary systems and the observational and theoretical challenges they present.

1.4.1 Keplerian Motion in Binary Systems

The motion of two bodies in a binary system, such as a pair of SMBHs in a binary AGN, can often be approximated by Kepler's laws of planetary motion, under the assumption that the gravitational interaction between the two bodies dominates over external forces. The Keplerian motion is described by:

$$F = \frac{Gm_1m_2}{r^2} \quad (1)$$

where F is the gravitational force between the two masses m_1 and m_2 , r is the separation between the two masses, and G is the gravitational constant. Kepler's third law, which relates the orbital period T to the semi-major axis a of the ellipse, is given by:

$$T^2 = \frac{4\pi^2 a^3}{G(m_1 + m_2)} \quad (2)$$

This equation allows for the determination of the masses of SMBHs in binary AGN systems based on their orbital period and separation.

1.4.2 Observational Signatures of Binary AGN

Detecting binary AGN systems poses significant observational challenges, primarily due to their compact separations and the need to disentangle the emissions from each AGN and their host galaxy. However, certain signatures can indicate the presence of a binary AGN:

1. **Dual Emission Lines:** Spectroscopic observations may reveal double-peaked emission lines, suggesting the presence of two distinct nuclei with their own accretion disks.
2. **Periodic Variability:** Periodic or quasi-periodic variations in the light curve of an AGN may indicate the orbital motion of binary SMBHs, affecting the accretion rate and thus the luminosity.
3. **Spatially Resolved Imaging:** High-resolution imaging, particularly in the radio band, can resolve the individual components of binary AGN systems, confirming their binary nature.

1.4.3 Evolution and Coalescence of Binary AGN

The intricate evolution of binary AGN comprises multiple stages, ultimately leading to SMBH coalescence. Understanding this process is essential for comprehending binary AGN dynamics and the mechanisms driving SMBH growth via mergers.

Dynamical Friction SMBHs' initial approach within their host galaxies is aided by dynamical friction. Interacting with stars and gas, each SMBH loses momentum, spiraling toward the merger remnant's center. This reduces the separation between SMBHs, facilitating binary system formation.

Hardening of the Binary After formation, the binary system hardens as interactions with stars and gas in the galactic nucleus shrink its orbit, increasing the SMBHs' orbital velocity and preparing them for merger.

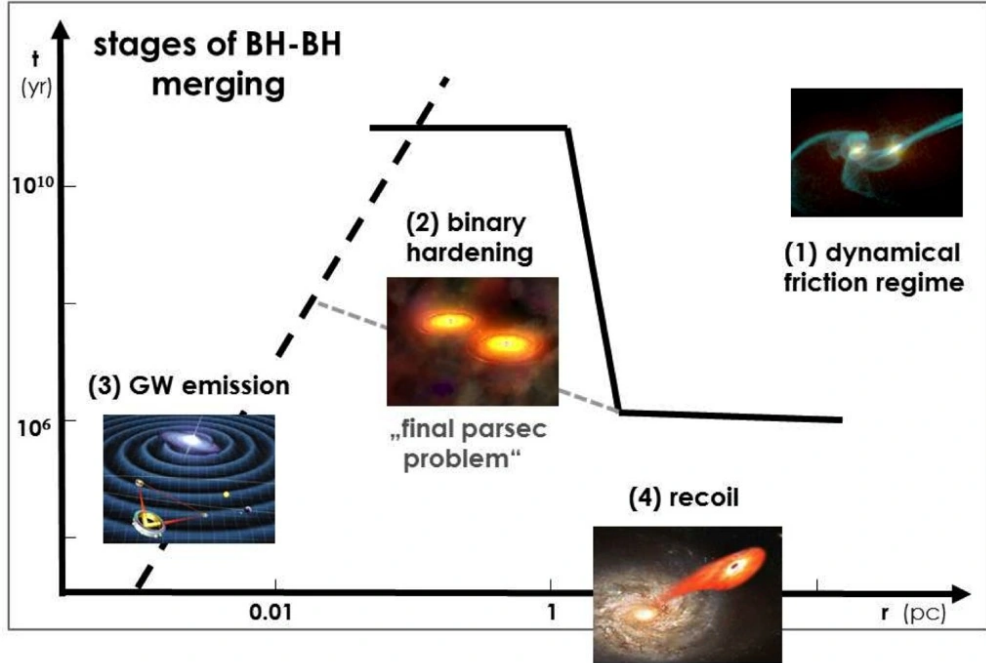


Figure 2: Stages of AGN/SMBH/BH-BH Merging <http://arxiv.org/abs/1502.05720>

Gravitational Wave Emission As SMBHs approach each other($\approx 1\text{lyr}$), GW emission becomes the dominant mechanism for orbital energy loss. This rapid inspiral culminates in coalescence, with the emitted gravitational waves potentially detectable by current and future observatories, providing direct evidence of SMBH mergers..

Gravitational Recoil As binary black holes merge, gravitational recoil can occur due to asymmetries in gravitational wave emission, potentially displacing the merged black hole. This effect has profound implications for SMBH demographics and galaxy evolution (Lousto and Zlochower, 2012). Understanding these processes is vital for interpreting observational signatures and predicting their impact.

CHAPTER 2: LITERATURE REVIEW

2.1 SMBH Dynamics, Galaxy Evolution, and Dual AGN Observations

Supermassive black holes (SMBHs), with masses between 10^6 and 10^9 solar masses, play a crucial role in galaxy evolution. Their correlation with host galaxy characteristics, such as bulge stellar velocity dispersion, highlights their influence on galactic dynamics (Ferrarese and Merritt, 2000; Gebhardt et al., 2000; Kormendy and Ho, 2013). Galaxy mergers are thought to be a key mechanism for SMBH growth and activity, supported by numerical simulations showing mergers trigger central gas inflows, fueling SMBHs and activating nuclear activity (Begelman et al., 2006; Di Matteo et al., 2005; Mayer et al., 2010). Evidence suggests major mergers contribute to the formation of luminous AGNs and quasar pairs, indicating interactions on cosmic scales (Fan et al., 2016; Hennawi et al., 2006; Treister et al., 2012).

Mid-IR, optical, and X-ray surveys have improved the detection of dual AGN, shedding light on the effects of gas-rich mergers on nuclear activation in galaxies (Foreman et al., 2009; Myers et al., 2008; Satyapal et al., 2014; Weston et al., 2017). Dual AGN serve as probes into merger processes, with their identification often requiring follow-up from wide-field surveys (Bhattacharya et al., 2023; Lusso et al., 2018; Shen et al., 2019).

X-ray observations are pivotal for studying dual AGN, as they can penetrate regions obscured to other wavelengths. The resolution of instruments like Chandra allows for the distinction of dual AGN at kiloparsec scales, essential for understanding the high-energy aspects of AGN activity (Fragos et al., 2013; Lehmer et al., 2016). This multi-wavelength approach to observing dual and binary AGN systems is key to unraveling the complex interplay between SMBHs, galaxy evolution, and the universe's energetic phenomena.

2.2 Supermassive Black Hole Binary Dynamics

Supermassive black hole binaries (SMBHBs) are central to galaxy evolution and merger dynamics, involving two SMBHs with sub-parsec separations. Despite observation challenges, theoretical, simulation-based, and indirect evidence insights into SMBHB formation, evolution, and properties

are significant (Begelman et al., 1980; Dotti et al., 2007; Khan et al., 2012; Mayer et al., 2007).

2.2.1 Theoretical Frameworks

SMBHB formation is anticipated when the combined black hole mass exceeds the mass of gas and stars within their orbit, typically under 10 pc separations. The evolutionary path, including star and gas dynamics, influences their coalescence (Begelman et al., 1980; Berczik et al., 2006; Merritt and Milosavljević, 2005; Yu, 2002).

2.2.2 Stellar and SMBH Interactions

The transition from stellar scattering to GW emission within a Hubble time faces the "last parsec problem," potentially mitigated by non-spherical galaxy potentials and anisotropies in stellar distributions, or interactions with a third SMBH, enhancing coalescence through Kozai-Lidov oscillations (Bonetti et al., 2018; Hoffman and Loeb, 2007; Khan et al., 2013; Milosavljević and Merritt, 2001; Preto et al., 2011; Ryu et al., 2018; Yu and Tremaine, 2003).

2.2.3 Gas Dynamics

Gas dynamics in post-merger galaxies may solve the final parsec problem, aiding SMBHB coalescence and predicting EM counterparts to GW signatures, with circumbinary disk interactions playing a crucial role (Armitage and Natarajan, 2002; Cuadra et al., 2008; Escala et al., 2005; Haiman et al., 2009).

2.2.4 Observational Challenges

Identifying SMBHB candidates relies on various techniques, with confirmation dependent on multiwavelength monitoring and theoretical validation (Fragos et al., 2013; Lehmer et al., 2016).

2.3 Future Perspective

Astrophysical research is on the brink of significant advancements in observing dual and binary AGN, with new ground- and space-based facilities spanning various energy bands promising to revolutionize our understanding from kpc-scale dual systems to sub-pc SMBHBs domains emitting

GW. Advances in numerical simulations of circumbinary disks and GW observations are setting the stage for direct SMBHB detections, enhancing our grasp on merger dynamics. Radio surveys, notably with the ngVLA, SKA, and VLASS, aim to comprehensively probe active black holes and dual-AGN cores through deep sky coverage and superior sensitivity (Burke-Spolaor, 2014; Nyland et al., 2018). Upcoming X-ray observatories, including eROSITA, Athena, AXIS, and Lynx, are expected to substantially expand the AGN population knowledge, especially at high redshifts, offering detailed insights into obscured AGN populations and young SMBHs (Merloni et al., 2012; Nandra et al., 2013). Optical spectroscopy, leveraging instruments like WHT/WEAVE and VISTA/4MOST, will focus on AGN characterization and dual AGN statistics among galaxy pairs (Bundy et al., 2015). Lastly, mid-IR advancements through JWST and the proposed SPICA mission will enrich our understanding of SMBH accretion physics and the early Universe (Rieke et al., 2015). Collectively, these efforts embody a multi-wavelength approach poised to unravel the complexities of AGN phenomena and evolution.

Table 2: Overview of Notable Astronomical Surveys

| Survey Name | Wavelength Band(s) | Primary Goals and Key Features |
|------------------------|---------------------------|---|
| SDSS | Optical, Infrared | Mapping the universe, studying the distribution of galaxies and quasars, Milky Way mapping. |
| HST Deep Field Surveys | Optical, UV, Infrared | Deep imaging of distant galaxies, universe structure, galaxy formation and evolution. |
| 2MASS | Near-Infrared | Celestial sky mapping, Milky Way structure, stellar populations. |
| CDFS | X-ray | Detecting black holes, galaxy clusters, X-ray background. |
| CANDELS | Near-Infrared | Galaxy formation and evolution from early universe, utilizing HST. |
| Gaia | Optical | Astrometry of Milky Way stars, three-dimensional galaxy mapping. |
| WISE | Mid-Infrared | Full sky mapping in infrared, discovering stars, galaxy morphology, AGN. |
| DES | Optical, Near-Infrared | Dark energy and matter, mapping galaxies, supernovae detection. |
| Planck | Microwave (CMB) | Mapping cosmic microwave background, studying early universe composition. |
| LSST | Optical | Mapping southern sky, dark matter and energy studies, cataloging solar system objects. |

CHAPTER 3: INSTRUMENTATION

3.1 Neil Gehrels Swift Observatory

The Neil Gehrels Swift Observatory, named in honor of the late astrophysicist Neil Gehrels, is a multi-wavelength space observatory dedicated to the study of gamma-ray bursts (GRB). Its versatile instruments allow for the observation of GRBs and their afterglows in the gamma-ray, X-ray, ultraviolet, and optical wavebands, providing comprehensive coverage of these cosmic phenomena.

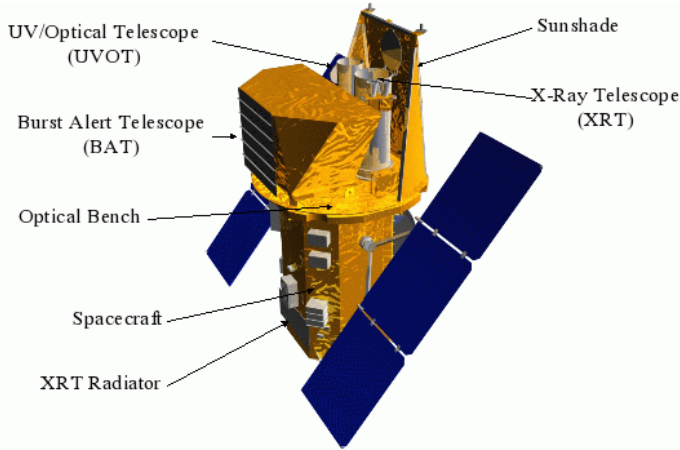


Figure 3: Schematic Diagram of Swift Observatory showcasing its main 3 telescopes, namely XRT, UVOT, and BAT. (Gehrels et al., 2004)

3.1.1 Swift/XRT (X-ray Telescope)

The X-ray Telescope (XRT) on board the Swift Observatory is designed for X-ray monitoring. It performs follow-up observations of GRBs detected by the Swift/BAT and provides detailed positional and spectral information. The XRT operates in the 0.3 to 10 keV energy range, capable of observing the afterglows of GRBs and other X-ray sources in the universe.

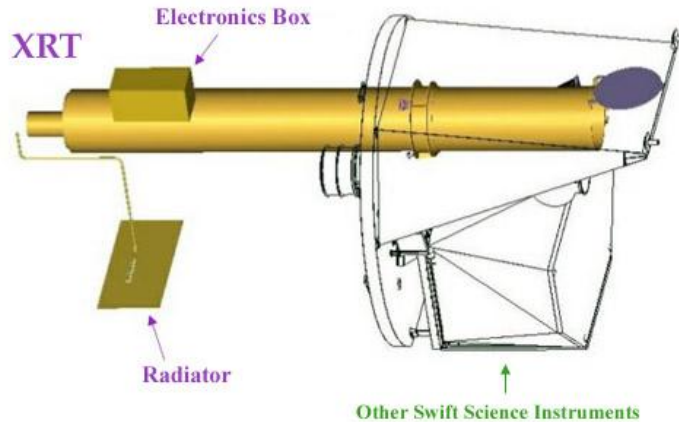


Figure 4: Schematic Diagram of XRT.(Burrows et al., 2005)

3.1.2 Swift/BAT (Burst Alert Telescope)

The Burst Alert Telescope (BAT) is the primary detection instrument on Swift, designed to quickly locate gamma-ray bursts and compute their coordinates in the sky. BAT operates in the 15-150 keV energy range and has a wide field of view, covering about one-sixth of the sky at any moment. Once BAT detects a GRB, Swift is maneuvered so that the GRB can be observed by both the XRT and the UVOT for detailed follow-up.

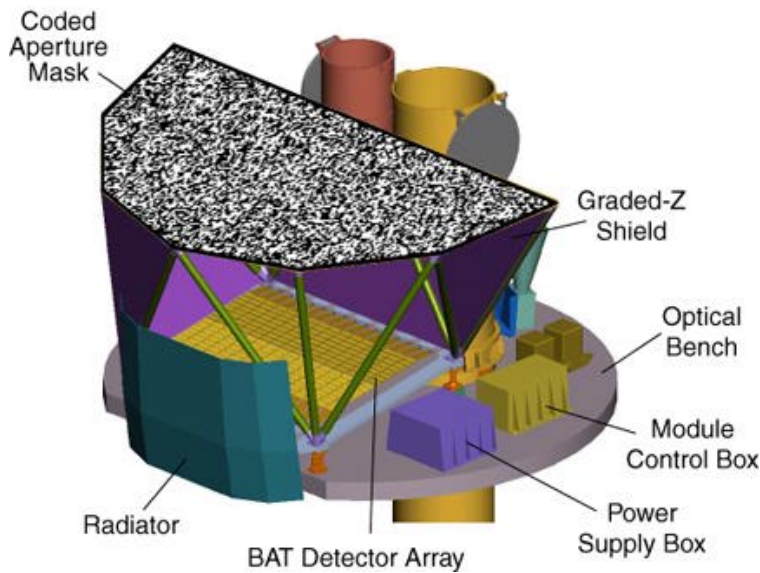


Figure 5: Schematic Diagram of BAT.(Barthelmy et al., 2005)

3.1.3 Swift/UVOT (Ultra-Violet/Optical Telescope)

The Ultra-Violet/Optical Telescope (UVOT) complements the XRT and BAT by providing observations in the ultraviolet and optical spectra. With a range of 170 to 600 nm, the UVOT is crucial for observing the afterglows of GRBs and obtaining precise positions, which can be distributed to observers on the ground for further study.

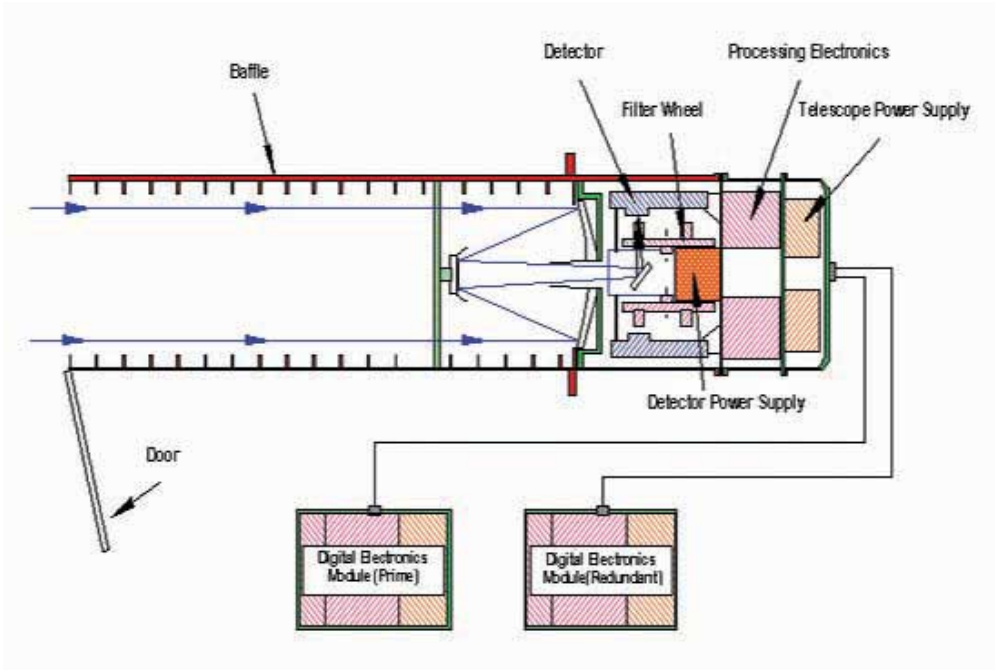


Figure 6: UVOT Layout. (Roming et al., 2005)

3.2 NuSTAR

The Nuclear Spectroscopic Telescope Array (NuSTAR) is the first space telescope capable of focusing X-rays at energies higher than those accessible to Swift and XMM-Newton, in the range of 3 to 79 keV. Its high-energy X-ray observation capabilities make it an invaluable tool for studying the extreme environments around black holes, supernovae, and other high-energy phenomena.

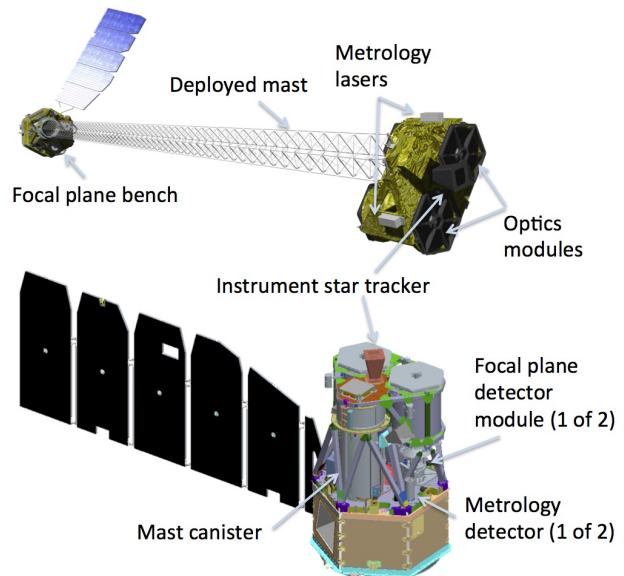


Figure 7: Schematic Diagram of NuSTAR X-ray Observatory. Credits: NASA/HEASARC Harrison et al., 2013

3.3 XMM-Newton

The XMM-Newton (X-ray Multi-Mirror Mission - Newton) is an ESA spacecraft launched in 1999, designed to observe high-energy phenomena such as black holes, neutron stars, and active galactic nuclei in the X-ray wavelength. With its large collecting area and capability to perform simultaneous optical/UV and X-ray observations, XMM-Newton plays a key role in our understanding of the X-ray universe.

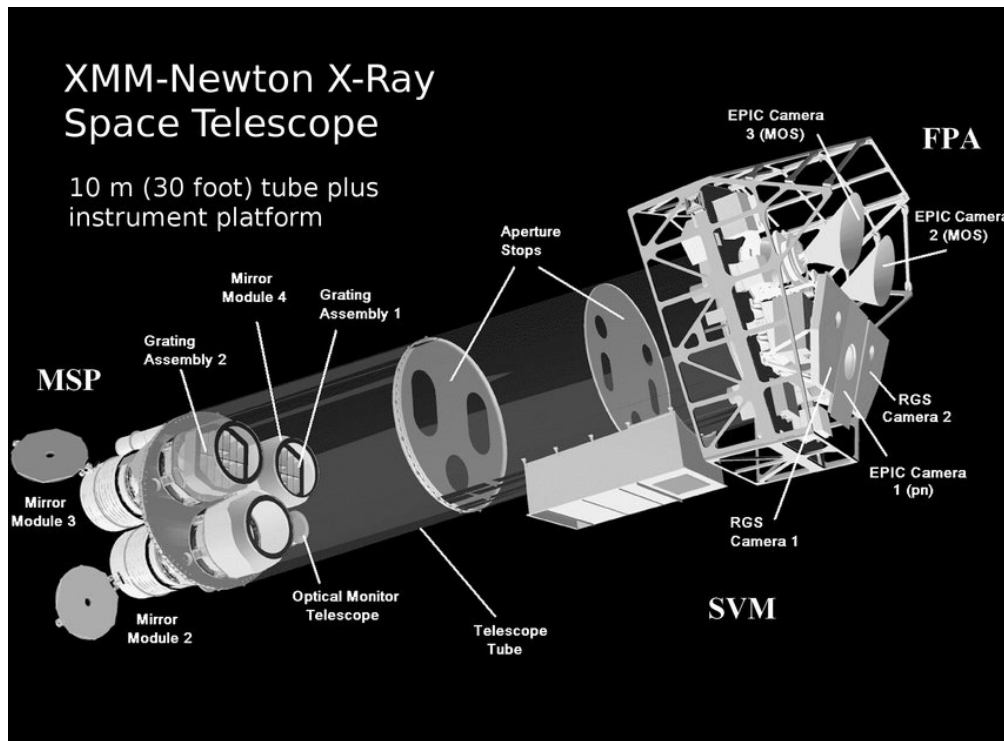


Figure 8: Schematic Diagram of XMM-Newton X-ray Observatory. Credits - ESA/XMM-Newton (*XMM-Newton Users Handbook*, 2021)

3.4 Chandra

The Chandra X-ray Observatory, named after the Nobel Prize-winning astrophysicist Subrahmanyan Chandrasekhar, is a NASA mission launched in 1999. It observes X-rays from high-energy regions of the universe, such as the remnants of exploded stars, clusters of galaxies, and matter around black holes. Chandra's high resolution allows it to resolve X-ray sources billions of light-years away.



Figure 9: The Chandra X-ray Observatory. Image Courtesy - NASA/Chandra(*Chandra Proposers' Observatory Guide*, 2021)

CHAPTER 4: RESEARCH METHODOLOGY

4.1 Building and Installing HEASoft Software

HEASoft, vital for high-energy astrophysics data analysis, is outlined in the following subsection. It provides a detailed installation guide for Linux systems, featuring precise commands for clarity.

1. To ensure compatibility and functionality of HEASoft, install the necessary dependencies. Execute the following commands based on your Linux distribution:⁵:

```
sudo apt update && sudo apt install -y zlib1g-dev libcurl4-openssl-
dev libxt-dev make gcc g++ \ gfortran perl python3-dev python3-
astropy python3-numpy python3-matplotlib
sudo -H pip3 install --upgrade scipy
```

2. Download the HEASoft package from the HEASARC website, choosing the version suitable for your system architecture and research requirements.⁶.
3. Unpack the downloaded HEASoft package in your preferred directory:

```
tar -zxvf heasoft-<version>.tar.gz
```

Replace <version> with the actual version number you downloaded.

4. Prior to the configuration, set environment variables to ensure the use of correct compilers:

```
export CC=/usr/bin/gcc
export CXX=/usr/bin/g++
export FC=/usr/bin/gfortran
```

⁵NASA's High Energy Astrophysics Science Archive Research Center. "How To Install HEASoft On Linux." <https://heasarc.gsfc.nasa.gov/docs/software/heasoft/install.html>.

⁶NASA's High Energy Astrophysics Science Archive Research Center. "HEASoft - Download (Version 6.33)." <https://heasarc.gsfc.nasa.gov/docs/software/heasoft/download.html>.

```
export PERL=/usr/bin/perl  
export PYTHON=/usr/bin/python3
```

5. Configure the HEASoft build environment to tailor the software compilation to your system specifications.

```
cd heasoft-<version>/BUILD_DIR/  
.configure > config.txt 2>&1
```

Output is logged into ‘config.txt’ for troubleshooting purposes.

6. Compile HEASoft by running the ‘make‘ command. Depending on your system’s capabilities and the selected HEASoft components, this step may take some time.

```
make > build.txt 2>&1
```

7. Install HEASoft onto your system. If the compilation is successful, proceed with:

```
make install > install.txt 2>&1
```

The ‘install.txt‘ file logs the installation process.

8. To make HEASoft available for use, initialize the HEASoft environment by setting the ‘HEADAS‘ environment variable to your installation path, and then source the initialization script.⁷:

```
export HEADAS=/path/to/your/installed/heasoft-<version>/(PLATFORM)  
source $HEADAS/headas-init.sh
```

⁷Jatan Mehta. "How to quickly install and setup NASA HEASoft on Ubuntu (or any Debian-based) Linux." <https://blog.jatan.space/p/how-to-quickly-install-and-setup-nasa-heasoft>.

Replace ‘/path/to/your/installed‘, ‘<version>‘, and ‘(PLATFORM)‘ with your actual installation path, version number, and system architecture, respectively.

This installation guide simplifies setting up HEASoft for high-energy astrophysics data analysis, enabling researchers to proceed efficiently with their scientific investigations.

4.2 Setting Up CALDB Environment

This section guides the setup of a local copy of CALDB, essential for high-energy astrophysics research, integrated with HEASoft for streamlined data analysis.

1. Define the environment variable \$CALDB to point to your calibration data directory. This is crucial for the system to locate and access the calibration data.
2. Download and install CALDB setup files by changing your working directory to \$CALDB and retrieving the necessary files from the HEASARC website. Uncompress and untar the setup files in your \$CALDB directory.
3. Configure the \$CALDB environment variables by sourcing the appropriate CALDB initialization file. For C-shell users, use
`source $CALDB/software/tools/caldbinit.csh;`
for Bourne shell users, use
`source $CALDB/software/tools/caldbinit.sh.`
4. To ensure the CALDB is accessible upon login, include the source command in your `.login` or equivalent initialization file.

```
> caldbinfo
Mode (BASIC, INST, or FULL) [ ]: INST
Name of Mission [ ]: SWIFT
Name of Instrument [ ]: XRT
```

```
** caldbinfo 1.0.2
... Local CALDB appears to be set-up & accessible
** caldbinfo 1.0.2 completed successfully
```

This command sequence verifies CALDB setup and accessibility for the SWIFT XRT instrument, confirming successful initialization.

For detailed guidance on downloading calibration data from HEASARC CALDB and incorporating non-HEASARC missions, consult HEASARC's CALDB documentation.⁸.

4.3 Data Reduction and Data Extraction

Data reduction and extraction are vital in X-ray astronomy, involving the conversion of raw data into a usable format for analysis. Data reduction aims to eliminate instrumental effects and background noise, ensuring accurate results. Data extraction involves processing relevant information like light curves and spectra to study astronomical objects. Given the complexity of X-ray data, advanced software tools are essential for effective analysis.

Significance in X-ray Astronomy In X-ray astronomy, data reduction and analysis play a crucial role due to observations' unique challenges. X-ray photons necessitate space-based observatories like SWIFT/XRT, SWIFT/BAT, XMM-Newton, NuSTAR, and Chandra. Calibration of instruments precedes data correction, tailored to each observatory's detectors and modes. Astronomers then filter and analyze data to isolate astrophysical signals, extracting time series, spectra, and spatial distributions.

These meticulous processes uncover insights into the universe's most energetic phenomena, including black holes, neutron stars, and galaxy clusters. X-ray astronomy, reliant on data reduction and analysis, is essential for advancing our cosmic understanding.

⁸Michael F. Corcoran and Lorraine Breedon, "How to Install a Calibration Database", <https://heasarc.gsfc.nasa.gov/docs/heasarc/caldb/install.html>

4.4 Swift/XRT

The Swift/XRT data reduction and analysis involve several steps to prepare the data for scientific interpretation. This process leverages the `xrtpipeline` for initial data processing, followed by image and spectral analysis using tools like `xselect`.

Initial Data Processing

The `xrtpipeline` command reprocesses raw data, applying calibration and standard filters:

```
xrtpipeline indir=<input_directory> outdir=<output_directory> \
srcra=<RA> srcdec=<DEC> steminputs=<obsid> clobber=NO
```

This step generates cleaned event files, ready for further analysis.

4.4.1 Creating Region Files

We need to create source and background region files manually. For that, we utilize SAO DS9 software.

1. Open Image in DS9

- Launch DS9.
- Open the image you want to analyze by selecting **File → Open** and navigating to your image file.

2. Display the Region Tool

- In the menu bar, go to **Analysis → Region**.
- A region control panel will appear.

3. Choose Region Shape

- Click on the region shape you want to create (e.g., circle, rectangle, annulus) in the

region control panel.

4. Draw Region on Image

- Click and drag on the image to draw the selected region shape.
- For circles, click once to define the center and drag to set the radius.
- For rectangles, click once to define one corner and drag to the opposite corner.



Figure 10: Selecting regions in DS9 using SWIFT/XRT Data

5. Save Region

- After creating and customizing regions, go to **Region → Save Regions** in the region control panel.
- Choose a location and filename for your .reg file, then click *Save*.

Extracting Images and Spectra

Using `xselect`, images and spectra are extracted from the cleaned event files. Commands within `xselect` allow for filtering events by energy or time, and extracting scientific products:

```
xselect> read events <cleaned_event_file>
```

```
xselect> filter <file_name> <min_energy>:<max_energy>
xselect> extract image/spectrum
xselect> save image/spectrum <output_image/spectrum>
```

Utilizing xrtproducts

The `xrtproducts` tool in Swift's data analysis suite efficiently generates spectra, ARFs, corrected light curves, and images from XRT event files. It's particularly adept at handling data from different observational modes, like Photon Counting (PC) and Windowed Timing (WT).

For a PC mode event file, `xrtproducts` can produce a spectrum, ARF, light curve, and image centered on given celestial coordinates with a specified radius and light curve bin size.

```
xrtproducts infile=sw00073125003xpcw2po_cl.evt stemout=DEFAULT regionfile=
DEFAULT outdir=./ binsize=100 ra=43.5645 dec=45.2048 radius=20 expofile=
sw00073125003xpcw2po_ex.img attfile=sw00073125003pat.fits
hdffile=sw00073125003xhdtc.hk
```

Each command leverages specific files (event, exposure maps, attitude, and housekeeping data) and parameters (RA, Dec, radius, binsize) to tailor the data products to the researcher's needs.

Similar process can be carried out for WT Mode.

4.4.2 ARF and RMF Creation

To construct Ancillary Response Files (ARFs), employ `xrtmkarf` with the exposure map, input spectrum, and output ARF name. Generating the Response Matrix File (RMF) is often automated in the data pipeline, with specifics available in the Swift/XRT user guide.⁹

Now the data is ready for spectral analysis in XSPEC.

For detailed instructions and further reading, consult the [Swift XRT Data Reduction Guide].¹⁰

⁹XRT Threads <https://www.swift.ac.uk/analysis/xrt/arfs.php>

¹⁰Swift XRT Data Reduction Guide: <https://www.swift.ac.uk/analysis/xrt/>

4.5 SWIFT/BAT

BAT Energy Conversion

Use bateconvert to ensure quadratic PHA to PI energy conversion for accuracy. Verify by checking GAINAPP and GAINMETH keywords with fkeyprint. If conversion is needed:

```
bateconvert infile=sw00377487000bevshsp_uf.evt ...
```

Producing a Quality Map and Applying Mask-Weighting

After ensuring the data is correctly processed, generate a Detector Plane Image (DPI) and define hot pixels using batbinevt and bathotpix. Then, apply mask-weighting with batmaskwtevt for accurate source positioning.

```
batbinevt infile=sw003774870000bevshsp_uf.evt outunits=counts ...
bathotpix infile=grb.dpi ...
batmaskwtevt infile=sw003774870000bevshsp_uf.evt ...
```

Creating Corrected Light-Curves and Images

For light-curves in energy bands between 15 and 350 keV:

```
batbinevt infile=sw00377487000bevshsp_uf.evt outunits=counts ...
```

Creating a Spectrum and Response Matrix

Extract a spectrum using batbinevt, then apply systematic error and update with batphasyserr and batupdatephakw. Build the response matrix file (RMF) with batdrmgen for spectral fitting.

```
batbinevt infile=sw00377487000bevshsp_uf.evt ...
batphasyserr infile=grb.pha ...
batupdatephakw infile=grb.pha ...
batdrmgen infile=grb.pha ...
```

For detailed analysis procedures and additional commands, consult the SWIFT/BAT analysis documentation.¹¹

¹¹SWIFT/BAT analysis documentation https://swift.gsfc.nasa.gov/analysis/bat_swguide_v6_3.pdf.

4.6 XMM-Newton

XMM-Newton's SAS is pivotal for processing and analyzing data from the XMM-Newton observatory. This section provides an overview of the SAS installation and the data reduction and analysis process.

4.6.1 SAS Installation

The SAS software facilitates the reduction, analysis, and interpretation of XMM-Newton data. Installation instructions and necessary files can be found on the XMM-Newton/SAS website.¹²

4.6.2 Data Preparation and Calibration

After installing SAS, the data preparation involves calibration and cleaning steps to convert raw observation data into a form suitable for scientific analysis. Calibration files of SAS can be downloaded from the official website¹³ or run the below command:

```
rsync -v -a --delete --delete-after --force --include='*.CCF' --exclude='*/'  
sasdev-xmm.esac.esa.int::XMM_VALID_CCF path/to/the/directory/
```

After initializing the SAS environment, two crucial commands are employed for preparing the data for analysis: `cifbuild` and `odfingest`.

- The `cifbuild` command is used to create the Calibration Index File (CIF) which is essential for the calibration of the observational data. It ensures that all subsequent analysis utilizes the correct calibration files.
- Following this, `odfingest` is executed to process the Observation Data Files (ODF), generating a summary file that contains vital metadata for the observation session. This step is necessary to align the data with the calibration information accurately.

These commands lay the groundwork for any further data reduction and analysis, ensuring that the data is correctly prepared and calibrated.

¹²<https://www.cosmos.esa.int/web/xmm-newton/sas-download>

¹³<https://www.cosmos.esa.int/web/xmm-newton/current-calibration-files>

4.6.3 Generating Cleaned Event Lists

The SAS commands `epchain` and `emchain` are instrumental in processing raw observation data from the EPIC-pn and EPIC-MOS cameras, respectively. These commands automate the calibration and creation of cleaned event lists, crucial for subsequent analysis.

```
epchain  
emchain
```

The Swift/XRT data reduction and analysis involve several steps to prepare the data for scientific interpretation. This process leverages the `xrtpipeline` for initial data processing, followed by image and spectral analysis using tools like `xselect`.

```
xmmextractor
```

This comprehensive approach ensures that the data from XMM-Newton's observations is accurately processed and ready for detailed scientific analysis.

4.6.4 Image and Spectral Analysis

SAS tools like `evselect`, `ds9`, and `especget` facilitate the extraction and analysis of images and spectra from the event lists.

```
evselect table=events.fits withimageset=yes imageset=image.fits  
ds9 image.fits  
especget eventset=events.fits spectrumset=spectrum.fits
```

This methodology outlines essential steps in XMM-Newton data reduction and analysis using SAS, with comprehensive details available in the XMM-Newton SAS-documentation.¹⁴

¹⁴<https://www.cosmos.esa.int/web/xmm-newton/sas-documentation>

4.7 NuSTAR Data Reduction and Analysis

NuSTAR's data framework is essential for analyzing raw X-ray data, with this section detailing its workflow and methods for better comprehension.

NuSTAR Data Overview NuSTAR data utilizes a structured observation ID (ObsID) format, nu[missionID] [targetID] [visitID], which encapsulates mission, target, and visit information. The data structure prioritizes efficiency, encompassing primary and secondary products such as raw telemetry, calibrated event files, and higher-level scientific data.

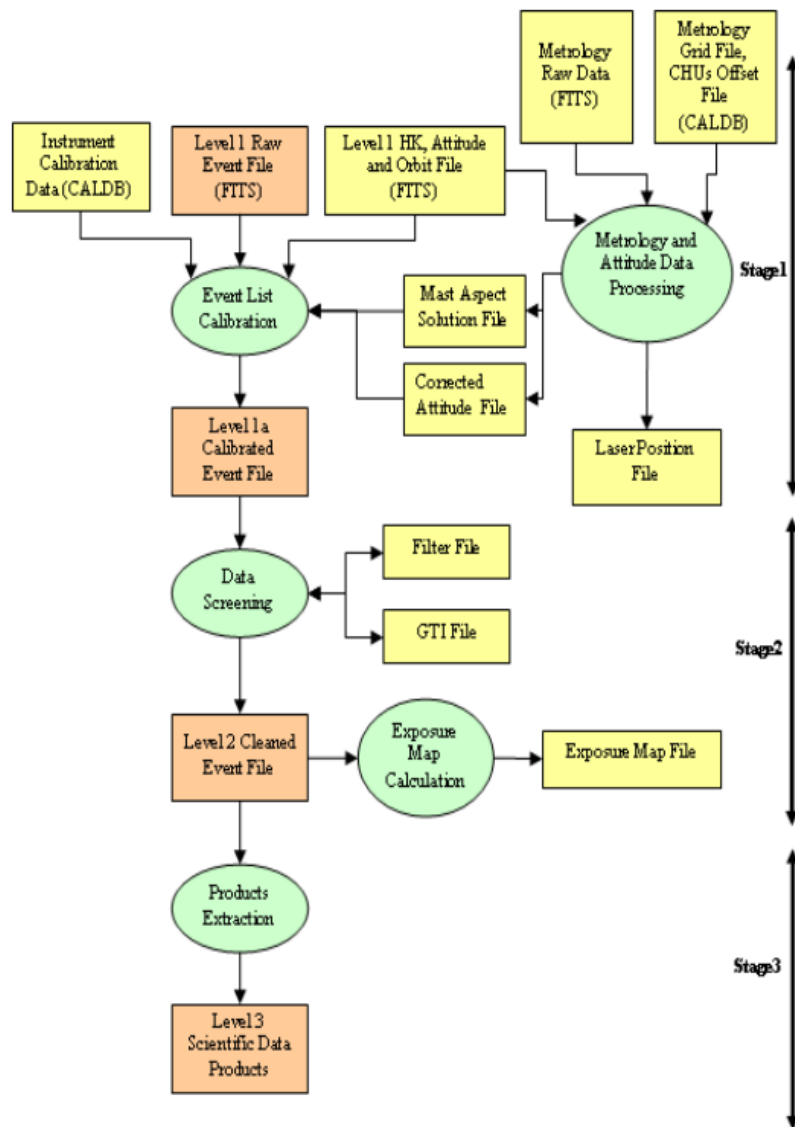


Figure 11: NuSTAR Data Structure Flowchart. Credits - HEASARC

Generating Level 2 Data Files with nupipeline The nupipeline script is instrumental in processing raw NuSTAR data into calibrated Level 2 data products, including the crucial cl_evt files.

```
nupipeline indir=/path/to/rawdata outdir=/path/to/level2data ...
steminput=/path/to/obsdir/nu60300021
```

This command initiates the calibration and cleaning processes, outputting data ready for scientific analysis.

Region File Creation in DS9 Creating accurate source and background region files is a critical step performed using the DS9 software. This process involves:

1. Opening the cl_evt.fits file in DS9.
2. Using DS9's analysis tools to identify and delineate source and background regions.¹⁵
3. Saving these regions for subsequent spectral and timing analysis.

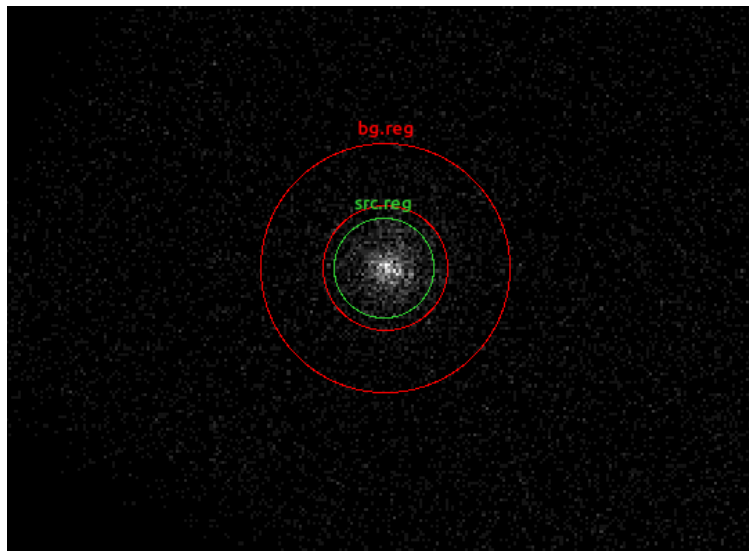


Figure 12: DS9 Region Selection Process using Nustar Image

FPMA and FPMB Telescope Specifications NuSTAR's FPMA and FPMB telescopes are pivotal in capturing high-energy X-ray data. Each telescope is equipped with a focal plane module

¹⁵Refer to section 4.4 for more details.

that consists of an array of detectors optimized for X-ray photon detection in the energy range of 3-79 keV.

Extracting Scientific Products with nuproducts The nuproducts tool facilitates the extraction of scientific products from Level 2 data files, utilizing the previously defined region files.

```
> nuproducts srcregionfile=source.reg bkgregionfile=bkg.reg indir=./  
outdir=./products steminputs=nu40060001001 instrument=FPMA runmkarf=no  
runmkrmf=no
```

This command generates spectra, light curves, and other key scientific data products essential for analysis.

Generating ARF and RMF Files with numkarf and numkrmf Accurate spectral analysis requires the generation of ARF and RMF, which are accomplished using numkarf and numkrmf commands respectively.

```
> numkarf phofile=nu40060001001A01_sr.pha outfile=nu40060001001A01_sr.arf  
optaxisfile=nu40060001001A_oa.fits offaxisfile=NONE offaxishisto=NONE  
apstophisto=NONE grhisto=NONE infile=nu40060001001A01_cl.evt  
attfile=nu40060001001_att.fits mastaspectfile=nu40060001001_mast.fits  
det1reffile=nu40060001001A_det1.fits  
  
> numkrmf infile=nu40060001001A01_cl.evt srcregionfile=source.reg  
outfile=nu40060001001A01_sr.rmf
```

Explanation:

- **phofile=nu40060001001A01_sr.pha:** Specifies the input file for the command, with the parameter name "phofile" followed by the filename "nu40060001001A01_sr.pha". This file contains spectral data.
- **outfile=nu40060001001A01_sr.arf:** Specifies the output file for the command, with the

parameter name "outfile" followed by the filename "nu40060001001A01_sr.arf". This file contains the resulting ancillary response file.

- `optaxisfile=nu40060001001A_oa.fits`: Specifies an optional axis file with the filename "nu40060001001A_oa.fits".
- `offaxisfile=NONE`: Specifies that no off-axis file is being used, as indicated by "NONE".
- `offaxishisto=NONE`, `apstophisto=NONE`, `grhisto=NONE`: Specify that certain histograms are not being used or generated, as indicated by "NONE".
- `infile=nu40060001001A01_cl.evt`: Specifies the input event file with the filename "nu40060001001A01_cl.evt" containing event data.
- `attfile=nu40060001001_att.fits`: Specifies the attitude file with the filename "nu40060001001_att.fits" containing spacecraft attitude information.
- `mastaspectfile=nu40060001001_mast.fits`: Specifies the mast aspect file with the filename "nu40060001001_mast.fits".
- `det1reffile=nu40060001001A_det1.fits`: Specifies a detector reference file with the filename "nu40060001001A_det1.fits".

These files are critical for calibrating the spectral energy response of the detectors, facilitating precise spectral analysis.

Further Analysis Subsequent analysis includes spectral fitting and timing analysis using tools like XSPEC.

This methodology outlines NuSTAR's data reduction and analysis steps, ensuring robust scientific insights from high-energy X-ray observations.

4.8 Chandra

4.8.1 CIAO Installation

The Chandra Interactive Analysis of Observations (CIAO) software is essential for the analysis of Chandra data. CIAO can be downloaded and installed by following the guidelines provided on the Chandra X-ray Center (CXC) website.

```
wget https://cxc.cfa.harvard.edu/ciao/download/ciao-install  
chmod +x ciao-install  
../ciao-install
```

Remember to source the CIAO configuration script in your shell profile to initialize the CIAO environment in every new terminal session.

Create Alias: Open the .bashrc using nano `~/.bashrc` in your home directory using a text editor.

Add the following line to the end of the file:

```
alias CIAO="/path/to/your/CIAOdir/ciao.sh"
```

Replace `/path/to/your/CIAOdir/ciao.sh` with the actual path to the `ciao.sh` script in your CIAO installation directory. Save the file and close the text editor. To apply the changes, either restart your terminal session or run the following command in your terminal: `source ~/.bashrc`

Now you can use the command `CIAO` in your terminal to execute the `ciao.sh` script from anywhere in your system. Sherpa, the spectral analysis software can also be used after the CIAO initialization.

4.8.2 Data Reduction and Analysis with CIAO

Data reduction in CIAO involves several steps, starting from the reprocessing of raw data to the extraction of scientific products like images and spectra.

Reprocessing Raw Data Use chandra_repro to reprocess the data, which applies the latest calibrations.

```
chandra_repro indir=/path/to/rawdata outdir=/path/to/reprodata
```

Image Analysis Creating and analyzing images is performed using tools like dmcopy and ds9.

```
dmcopy "infile[energy=500:7000]" outfile=image.fits  
ds9 image.fits
```

Spectral Analysis Extracting and analyzing spectra involve commands like specextract.

```
specextract infile="reprodata/*evt2.fits[sky=region(src.reg)]"  
outroot=my_source_spec bkgfile="reprodata/*evt2.fits[sky=region  
(bkg.reg)]"
```

Note: For the generation of region files, one can simply use SAO DS9. Although Chandra_repro creates src.reg and bg.reg files already, it is advisable to generate the required region files manually by opening *evt2.fits in DS9.

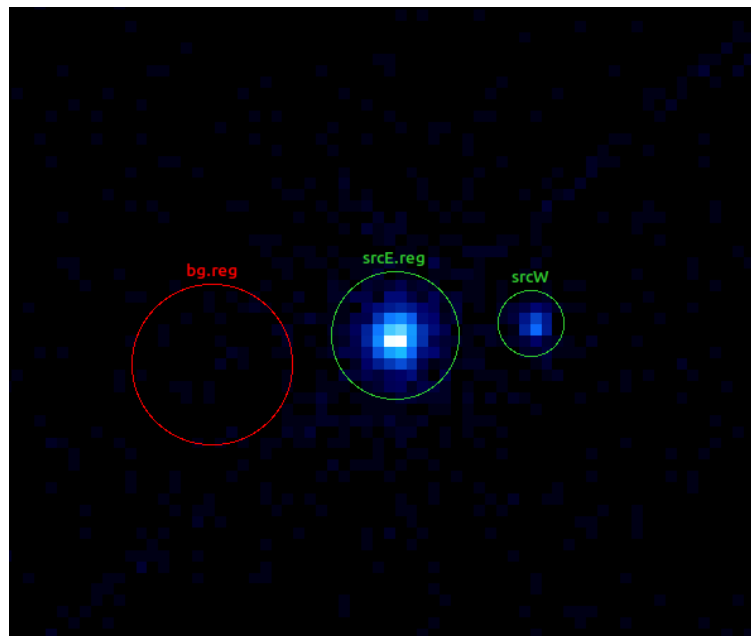


Figure 13: DS9 Region Selection Process with Chandra image

The extracted spectra "src.grp.pi" can be analyzed in XSPEC/Sherpa.

This section details the process for installing CIAO and managing CXO data reduction emphasizing the importance of each command and step in deriving scientific insights from high-energy astronomical observations.

SPECTRAL ANALYSIS

Spectral analysis, crucial for understanding celestial objects' physical properties and compositions in astrophysics, utilizes tools like XSPEC and Sherpa. These provide frameworks for fitting theoretical models to observed spectra.

4.9 XSPEC Analysis

XSPEC is a command-driven software that allows for the fitting of astronomical X-ray spectra. The process begins with loading the observation data and background spectra into XSPEC:

```
XSPEC> data observation.pha  
XSPEC> background background.pha
```

A model is then defined, for example, an absorbed power-law for a source:

```
XSPEC> model tbabs*powerlaw
```

The fitting process iteratively adjusts model parameters to minimize discrepancies between the observed data and the model.

For detailed guidelines on spectral analysis with XSPEC, refer to the official documentation provided by the [XSPEC]¹⁶.

¹⁶<https://heasarc.gsfc.nasa.gov/xanadu/xspec/>

4.10 Understanding the Spectrum

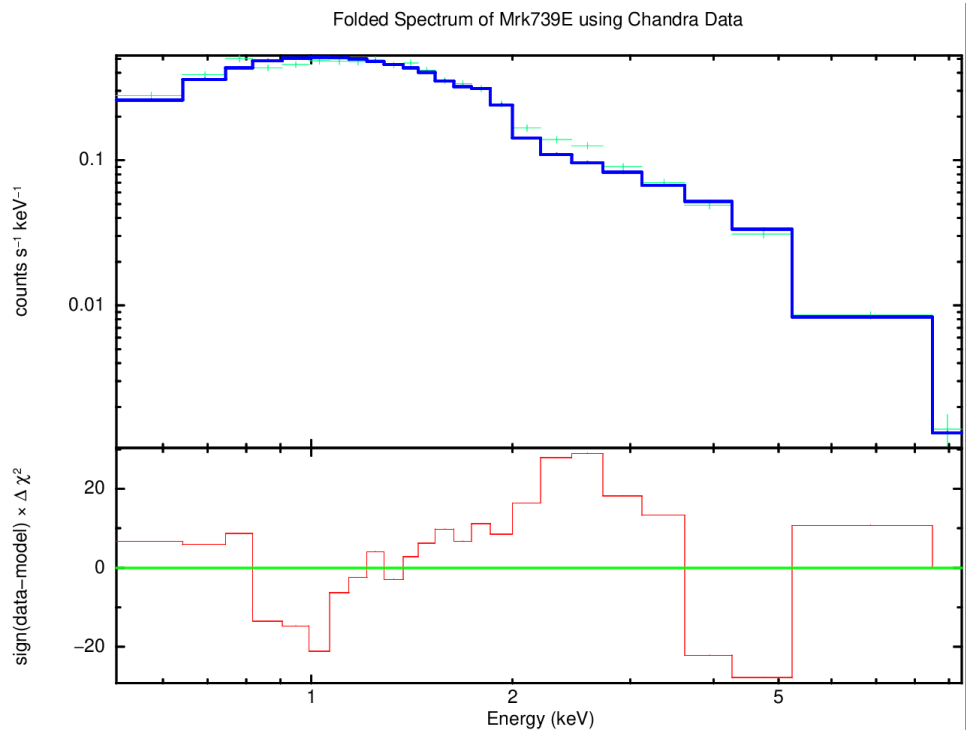


Figure 14: Example of an X-ray spectrum fitted with an absorbed power-law model. Key features include the continuum shape determined by the power-law and absorption edges modeled by tbabs.

Figure 14 illustrates a typical X-ray spectrum. The x-axis represents the energy of the photons, typically in keV, while the y-axis shows the counts or flux. The continuum's shape is defined by the power-law component, indicating the source's spectral slope. Absorption features, such as edges or lines, may indicate interstellar material's presence along the line of sight.

IMAGE ANALYSIS

4.11 Calculating the Nuclear Separation of the Dual AGN

In analyzing the AGN, an essential aspect is determining the physical separation between the two nuclei. Given the celestial coordinates in RA and Dec for each AGN, we aim to estimate this separation. The process involves several conversion and calculation steps, utilizing the Pythagorean theorem as an approximation under the assumption of small angular distances.

4.11.1 Coordinate Conversion

The celestial coordinates are given in HH:MM:SS for RA and DD:MM:SS for Dec. The first step is converting these into decimal degrees:

$$\text{Decimal Degrees} = \left(HH + \frac{MM}{60} + \frac{SS}{3600} \right) \times 15 \quad (3)$$

for RA, where 1 hour equals 15 degrees, acknowledging the 24-hour rotation period of the Earth.

For Dec, the conversion is straightforward:

$$\text{Decimal Degrees} = DD + \frac{MM}{60} + \frac{SS}{3600} \quad (4)$$

4.12 Calculating Angular Separation

4.12.1 Using Pythagorean Theorem

Assuming a small angular separation, we employ a flat-sky approximation for simplicity. The difference in RA, adjusted for the cosine of the average declination, and the difference in Dec are used as the perpendicular sides of a right triangle. The separation, d , is the hypotenuse, calculated using the Pythagorean theorem:

$$d = \sqrt{(\Delta RA \cdot \cos(\bar{Dec}))^2 + (\Delta Dec)^2} \quad (5)$$

where ΔRA is the difference in RA between the two AGNs converted to degrees, ΔDec is the difference in Declination, and \bar{Dec} is the average Declination of the two AGNs.

Note: The $\cos(\bar{Dec})$ factor scales the RA difference to account for the varying physical distance a degree of RA represents at different declinations, ensuring accurate calculation of the physical separation on the celestial sphere's surface.

4.12.2 Using the Spherical Law of Cosines

Given the declinations (δ_1, δ_2) and right ascensions (α_1, α_2) of the two AGNs, the angular distance d between them on the celestial sphere is calculated using the spherical law of cosines:

$$\cos(d) = \sin(\delta_1) \sin(\delta_2) + \cos(\delta_1) \cos(\delta_2) \cos(\Delta\alpha) \quad (6)$$

where $\Delta\alpha = \alpha_2 - \alpha_1$ is the difference in right ascension between the two AGNs.

4.12.3 Conversion to Physical Units

To estimate the physical separation between the two AGNs, we first determine the distance to the AGN pair using the cosmological redshift, z . The distance D to the object in a cosmological context can be calculated using the redshift and a cosmological model, such as the Lambda Cold Dark Matter (ΛCDM) model. For simplicity, we can use Hubble's law in the nearby universe approximation:

$$D = \frac{c \cdot z}{H_0} \quad (7)$$

where c is the speed of light (3.00×10^5 km/s), H_0 is the Hubble constant (approximately 70 km/s/Mpc), and z is the redshift. Given z , we calculate D .

Once D is known, the linear separation L between the two AGNs, in parsecs, can be derived from the angular separation d (calculated previously) using the small angle formula, which is more appropriate for astronomical distances:

$$L = 2 \cdot D \cdot \sin\left(\frac{d}{2}\right) \quad (8)$$

Here, d is the angular separation in radians, and L provides the physical distance between the dual AGNs in parsecs. This calculation offers an insightful measure of the scale of interaction and the physical dynamics of the dual AGN system.

4.12.4 Python Code for Calculating Nuclear Separation of dual AGN

Below is the Python code used to calculate the angular distance between two points on the celestial sphere, given their Right Ascension (RA) and Declination (Dec) in hours, minutes, seconds, and degrees, minutes, seconds respectively.

```
from math import sin, cos, acos, radians

# Helper function for RA and Dec conversion
def ra_to_decimal(hours, minutes, seconds):
    return (hours + minutes / 60 + seconds / 3600) * 15

def dec_to_decimal(degrees, arcminutes, arcseconds):
    return degrees + arcminutes / 60 + arcseconds / 3600

# Eastern AGN coordinates in decimal degrees
ra_eastern_deg = ra_to_decimal(11, 36, 29.3555)
dec_eastern_deg = dec_to_decimal(21, 35, 46.173)
```

```

# Western AGN coordinates in decimal degrees
ra_western_deg = ra_to_decimal(11, 36, 28.9322)
dec_western_deg = dec_to_decimal(21, 35, 46.656)

# Convert to radians
ra_eastern_rad = radians(ra_eastern_deg)
dec_eastern_rad = radians(dec_eastern_deg)
ra_western_rad = radians(ra_western_deg)
dec_western_rad = radians(dec_western_deg)

# Calculate the difference in right ascension in radians
delta_alpha_rad = abs(ra_eastern_rad - ra_western_rad)

# Calculate angular distance using the spherical law of cosines
cos_d = sin(dec_eastern_rad) * sin(dec_western_rad) + cos(dec_eastern_rad) *
cos(dec_western_rad) * cos(delta_alpha_rad)
d_rad = acos(cos_d)

# Convert angular distance from radians to arcseconds for interpretation
d_arcsec = d_rad * (206265) # 1 radian = 206265 arcseconds

d_arcsec

```

This neat python code gives us the value of nuclear separation between two AGN in arcsec('').¹⁷

¹⁷For further information about the code, check my github repository https://github.com/Ash-heheh/Dual_AGN_Nuclear_Separation.git

4.13 RA and DEC Observations

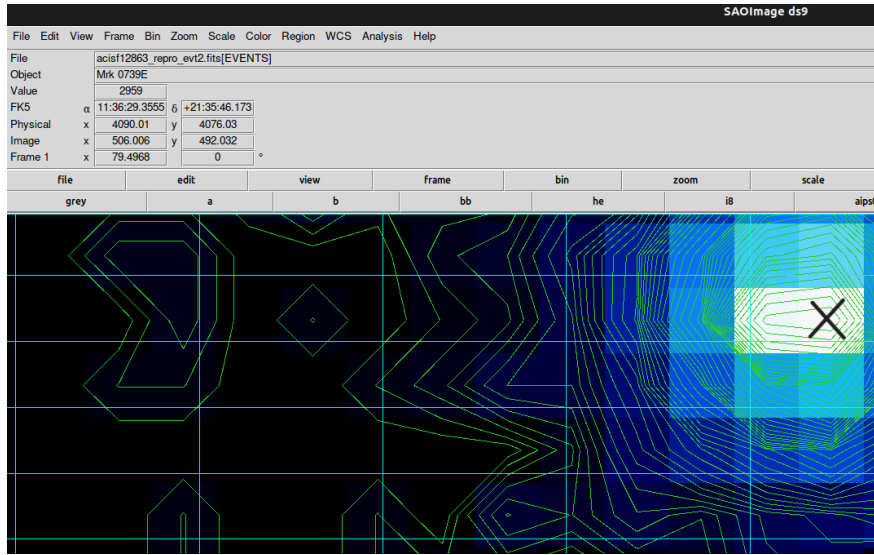


Figure 15: Mrk739 Eastern Component

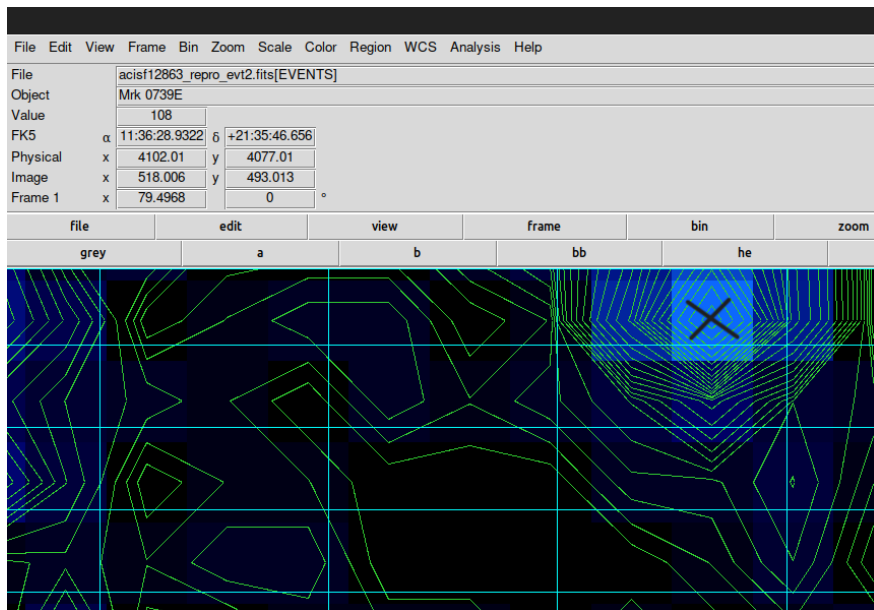


Figure 16: Mrk739 Western Component

| | Source | RA | DEC |
|---------|---------------|---------------|-----|
| Mrk739E | 11:36:29.3555 | +21:35:46.173 | |
| Mrk739W | 11:36:28.9322 | +21:35:46.656 | |

Table 3: RA and DEC Observations for Mrk739 Components

CHAPTER 5: RESULTS AND DISCUSSION

IMAGE ANALYSIS

We used Chandra's superior resolution power ($0.5''$) to resolve dual AGN Mrk 739, as shown below:

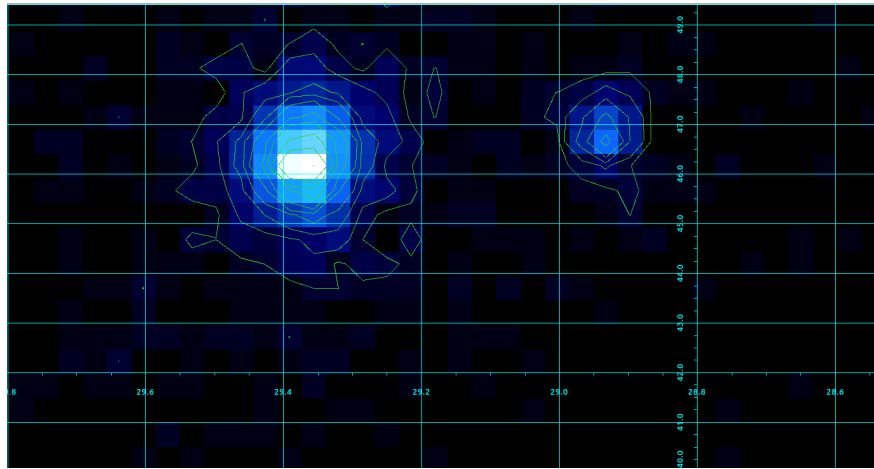
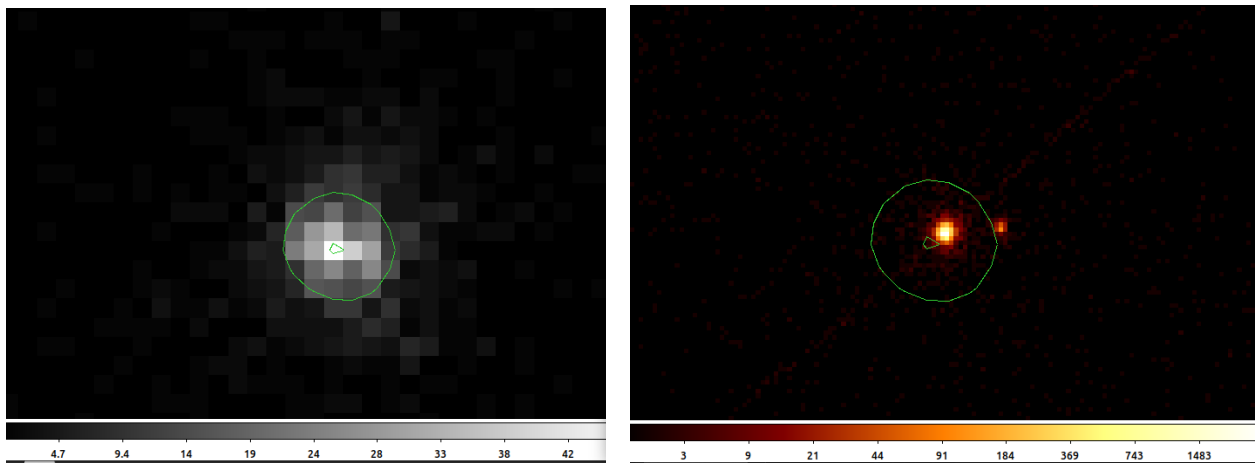


Figure 17: Mrk 739 East (left) and Mrk 739 West (right) as resolved by Chandra's High-Resolution Camera on the ACIS/S. The contours illustrate intensity levels across the RA and DEC grid.

Below we can see the limitations of X-ray observatories like SWIFT Observatory in resolving dual AGN like objects. However, Chandra ACIS/S with its 0.5 arcsecond ($2.4 \mu\text{rad}$) resolution power can resolve both the AGN properly.



(a) SWIFT/XRT image of Mrk 739.

(b) Chandra ACIS/S Image of Mrk 739.

Figure 18: Comparison of SWIFT/XRT and Chandra ACIS/S images of Mrk 739.

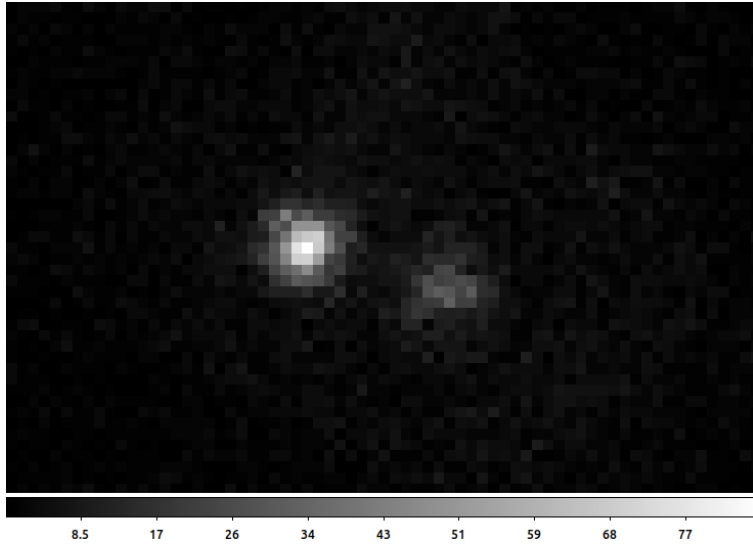


Figure 19: XMM-Newton/OM Image of Mrk739.¹⁸

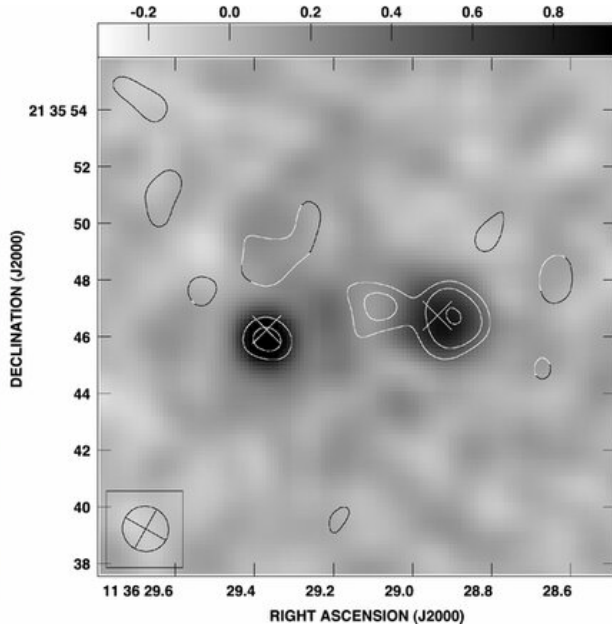


Figure 20: Grey-scale image is the 1.49 GHz VLA data, while the contours are the 4.86 GHz data convolved to 1.49 GHz beam. White x's indicate the Chandra hard X-ray positions. Credits - Koss et al.¹⁹

¹⁸The observed variation in orientation within the OM image can be attributed to misalignment and the absence of calibration with the standard celestial coordinate system. However, for the purposes of this study, these variations are not of concern.

¹⁹Koss, M., et al. "Chandra Discovery of Binary AGN Mrk 739." We refered this paper to access the Radio Image See <https://arxiv.org/abs/1106.2163> for more details. Please note that this radio image was utilized for comparative analysis with the extracted X-ray data.

Below we present Chandra ACIS/S images of other dual AGN and dual AGN candidates:

1. **J133817.7+481634/Mrk 266/NGC 5256**: Mrk 266 is a fascinating example of a dual AGN, situated within the constellation Canes Venatici. With a redshift of ≈ 0.0279 , Mrk 266 is about 129 Mpc away from Earth, presenting a unique opportunity to observe the dynamics of galaxy interaction and AGN activity up close. The system's dual nuclei are separated by 10 arcseconds or about 6 kpc (refer Table 4).

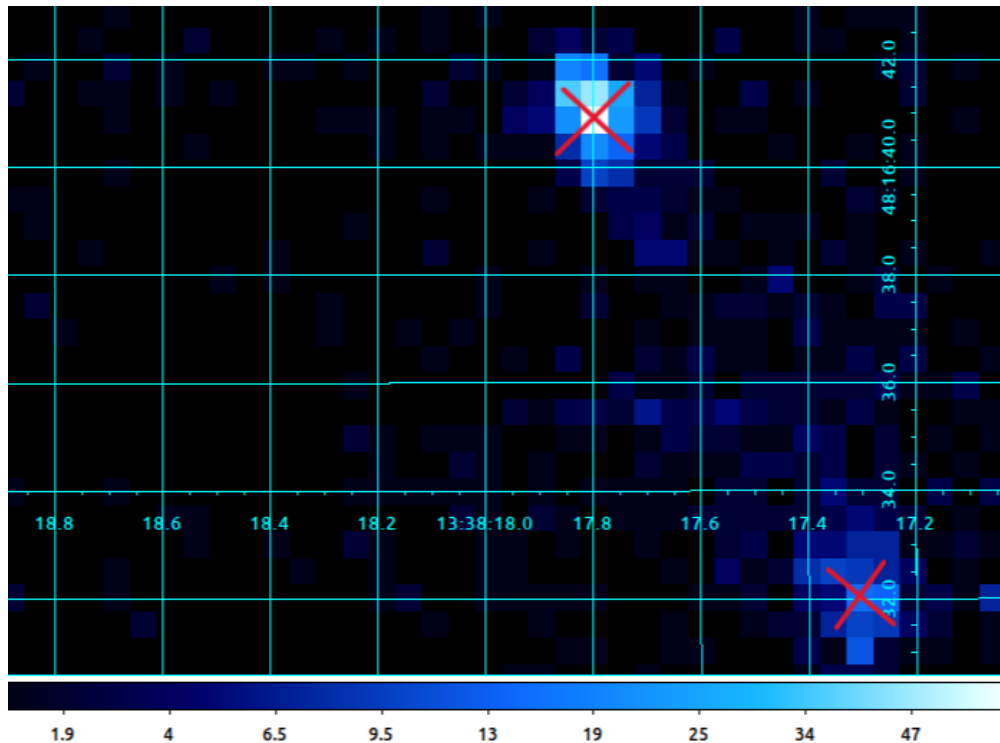


Figure 21: The Chandra ACIS/S image of the dual AGN, Mrk 266, is depicted alongside a standard RA DEC coordinate grid. Cross marks denote the predicted positions of the AGN, coinciding with regions exhibiting the highest intensity of X-ray emission.

2. J125929.9+275723 (within Comma Cluster): The dual AGN J125929.9+275723, exists within Comma Cluster (Rosa et al., 2022).²⁰ This dual AGN, with an approximate redshift of 0.0227, exhibits a projected nuclear separation of approximately 26 kpc(refer Table 4).

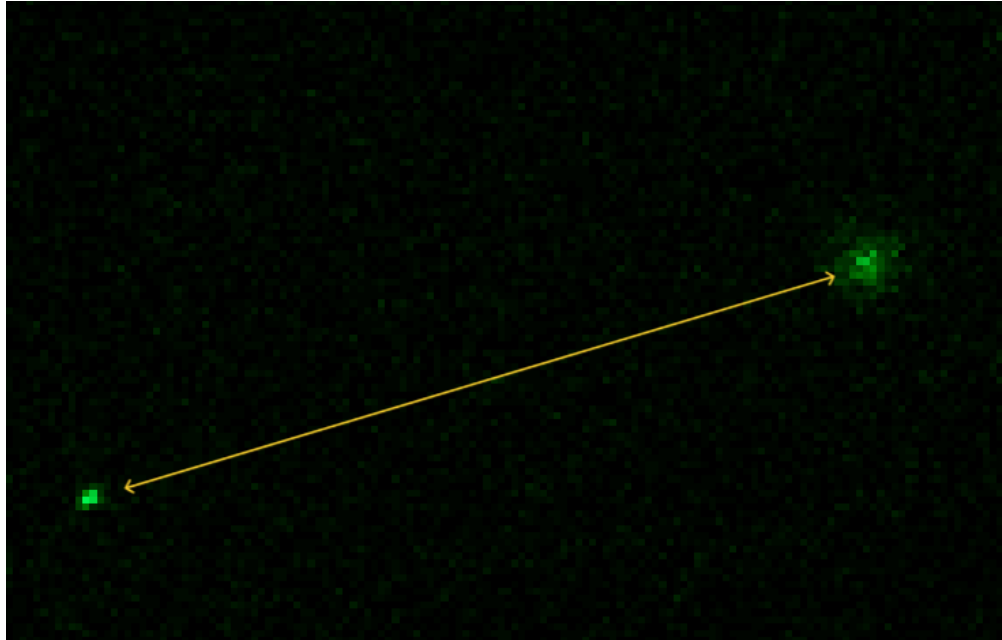


Figure 22: The Chandra ACIS/S image of the candidate dual AGN, J125929.9+275723.

²⁰“The X-ray view of optically selected dual AGN” Rosa et al.<https://academic.oup.com/mnras/article/519/4/5149/6912275>

3. J135602.9+182219/Mrk 463: Prominently featured in the constellation of Canes Venatici, Mrk 463 stands out as a key system in the exploration of dual AGN. Known for its intricate dynamics resulting from a late-stage gas-rich major galaxy merger, Mrk 463 offers a remarkable laboratory for studying the complex interplay between gas dynamics, star formation, and SMBH accretion. This system, lying at a distance of approximately 210 Mpc²¹ from Earth, showcases a nuclear separation of about 3.8 kpc (refer Table 4), underlining the close yet distinct nature of its dual AGNs.

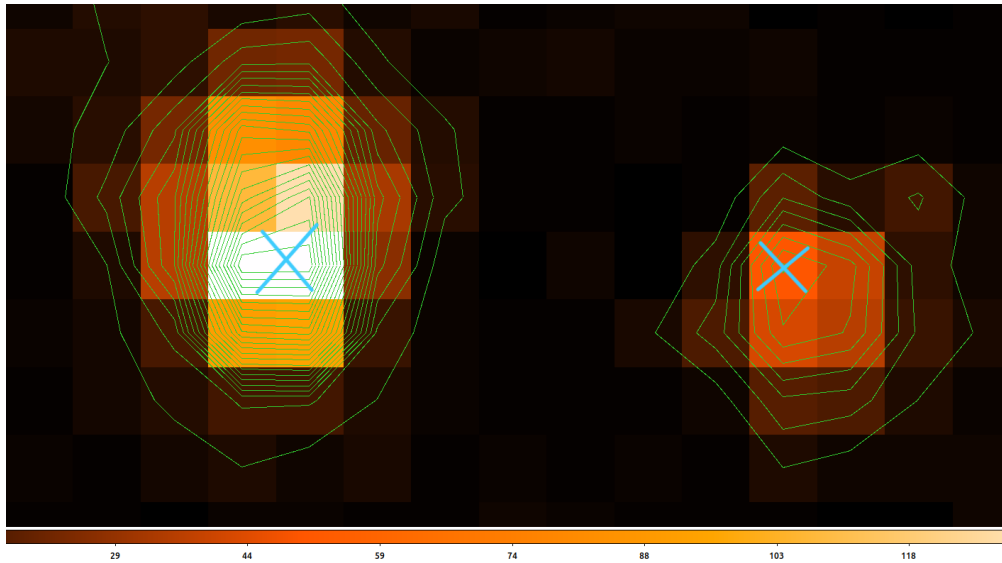


Figure 23: The Chandra ACIS/S image of the candidate dual Active Galactic Nuclei (AGN), Mrk 463, is presented with contours indicating X-ray intensity levels. Cross marks overlay the image, indicating the predicted positions of the AGN, which correspond to regions of highest X-ray emission intensity.

²¹”Chandra unveils a binary active galactic nucleus in Mrk 463” Bianchi et al 2008 <https://academic.oup.com/mnras/article/386/1/105/977141>

4. J165258.9+022403.3/NGC 6240: Located in Ophiuchus, NGC 6240 exemplifies galactic mergers and is notable for its Binary AGN (Komossa et al., 2003). At a redshift of $z = 0.0245$, it offers a rare view into SMBH interaction and coalescence within a few thousand light-years/less than 1kpc (see Table 4). This system is invaluable for studying gravitational dynamics in galactic mergers and contributes significantly to our understanding of galaxy evolution, star formation, and black hole growth.²²

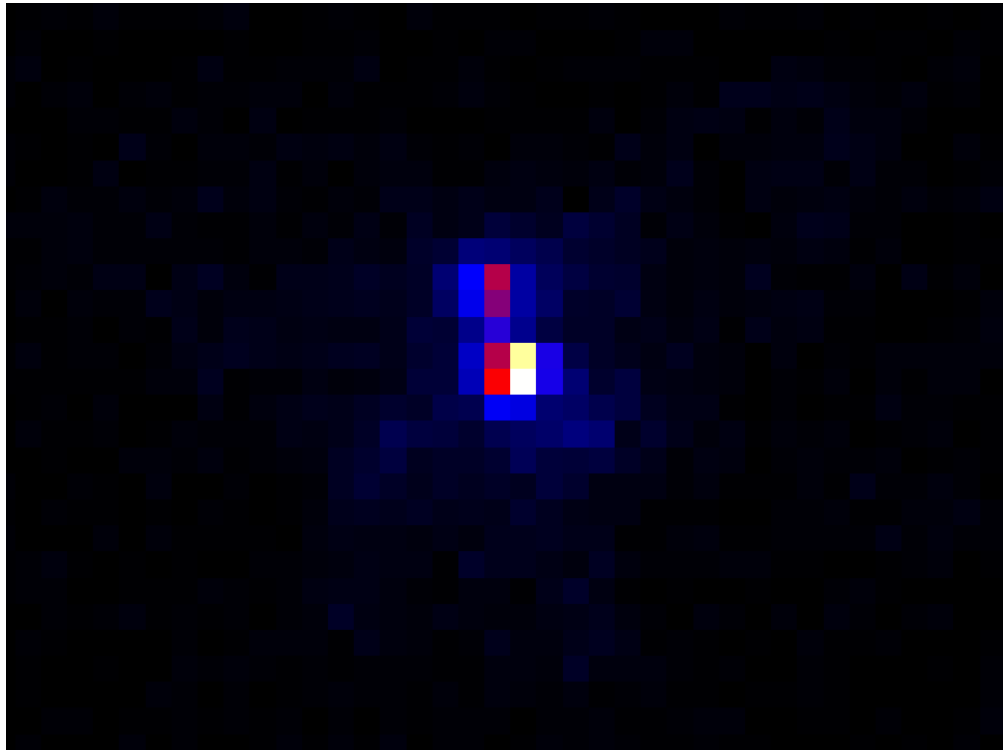


Figure 24: The Chandra ACIS/S image of the candidate dual Active Galactic Nuclei (AGN), NGC6240

²²"Nuclear absorption and emission in the AGN merger NGC 6240: the hard X-ray view" Emanuele Nardini 2017
<https://doi.org/10.1093/mnras/stx1878>

NGC 7674/Mrk 533 Dual AGN Potential: In Pegasus, NGC 7674 (Mrk 533) is central to dual AGN studies, potentially hosting a sub-parsec SMBHB (M. J. Koss et al., 2017), with two SMBHs separated by only 0.35 parsecs. This finding underlines its importance in understanding dual AGN mechanisms and their impact on galaxy evolution and SMBH interactions. Although Chandra cannot directly resolve this binary, other data imply NGC 7674 may have a dual/multiple AGN companion, creating an intriguing case for dual/multiple AGN presence with a nuclear separation of $\approx 37\text{kpc}$ (see Table 4 and Figure 25), though it's a less pronounced example of multiple AGN.



Figure 25: The Chandra ACIS/S image displays the dual AGN, NGC 7674, situated in the southern region of the image. Additionally, a potential companion AGN is observed in the northern portion of the image.)

J131517.3+442425/UGC08327 Dual AGN Prospect: This source hints at a dual AGN presence, but the North component's low counts call for additional observations and multiwavelength analysis to confirm its dual AGN status. Hence, making conclusive statements about nuclear separations from the current data alone is premature.

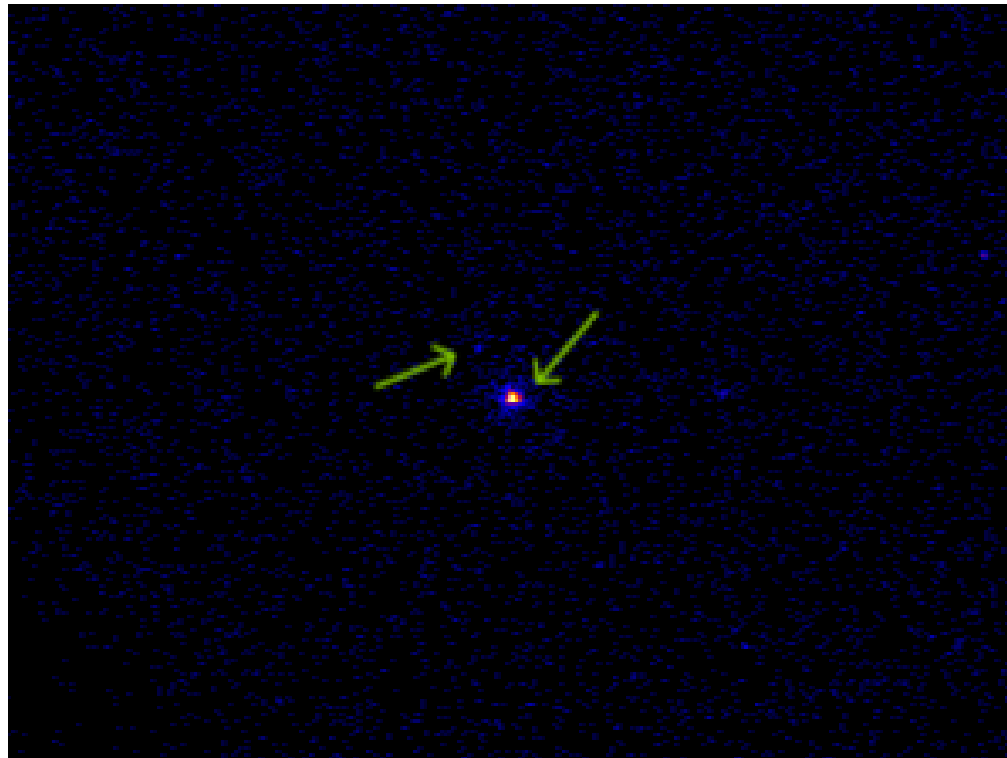


Figure 26: The Chandra ACIS/S image of the candidate dual AGN, J131517.3+442425

UGC 4211 Dual AGN Dynamics: Situated in a late-stage major merger, UGC 4211 presents a highly compact dual AGN system with a nuclear separation of ≈ 230 parsecs ($z = 0.03474$), offering a window into merger dynamics and SMBH coalescence. However, Chandra's $\sim 0.5''$ resolution limits exploration of such closely separated AGNs, as it can resolve separations of ~ 360 parsecs or greater at ~ 0.0344 , challenging for analyzing UGC 4211's finer separations.

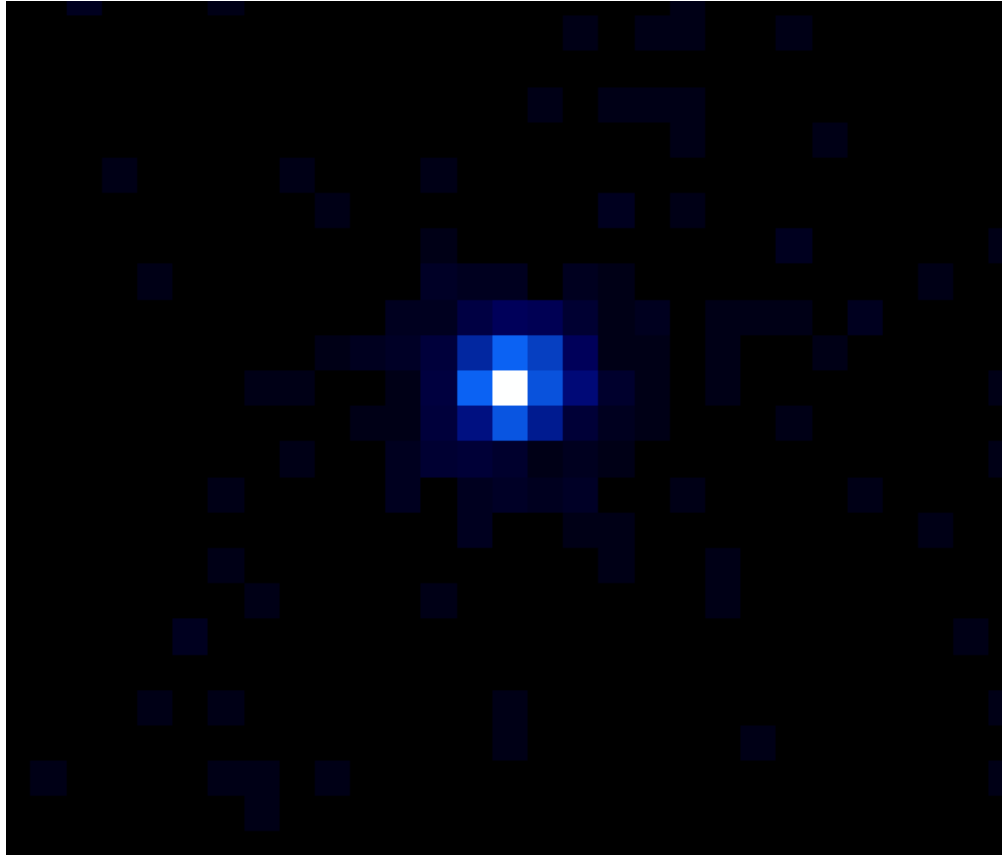


Figure 27: The Chandra ACIS/S image of the candidate dual AGN, 4211.

As we can see here, UGC 4211 and UGC 08327 represent constraints or limitations within the methodology being employed.

5.1 Projected Nuclear Separation

Table 4: Observational Data Summary

| Obs ID | Simbad Name | Redshift (z) | Projected Angular Separation | Projected Nuclear Separation (kpc) | Nu- clear Separation (arcsec) | Other Names |
|--------|---------------------|------------------------|------------------------------|------------------------------------|----------------------------------|-------------|
| 12863 | J113629+213546 | $0.029771 \pm 1.00e$ | 5.877 ± 0.05 | 3.63 ± 0.03 | Mrk739 | |
| 2044 | J133817.7+481634 | $0.027863 \pm 4.30e-5$ | 10.203 ± 0.05 | 5.90 ± 0.053 | Mrk266/ NGC5256 | |
| 4913 | J135602.9+182219 | $0.050802 \pm 4.70e-5$ | 3.664 ± 0.05 | 3.7557 ± 0.0581 | Mrk 463 | |
| 6908 | J165258.9+022403.3 | $0.024307 \pm 2.70e-5$ | 1.94282 ± 0.05 | 0.92661 ± 0.0673 | NGC 6240 | |
| 13996 | J125929.9+275723 | 0.0227 ± 0.0003 | 55.9067 ± 0.55 | 26.6423 ± 0.899 | Coma Cluster | |
| 22089 | ★J080446.39+104636 | $0.034434 \pm 1.90e-4$ | NA | NA | UGC4211 | |
| 12242 | ★J131517.3+442425 | $0.035522 \pm 1.22e-5$ | NA | NA | UGC08327/ Mrk248 | |
| 23715 | †J232756.7+084644.3 | $0.029030 \pm 5.00e-6$ | 63.1022 ± 0.55 | 37.8983 ± 0.899 | NGC 7674 | |

★ denotes the limitation of Chandra's superior resolution, indicating constraints on the methodology presented in Chapter 3 (Research Methodology) for image analysis. † denotes candidates that cannot be resolved in Chandra, optionally considering another possible dual/multiple AGN companion of the dual AGN.

The table summarizes the results of image analysis of dual AGN and dual AGN candidates.²³

²³These sources were selected based on the findings presented in the paper titled "The X-ray view of optically selected dual AGN" by Rosa et al., 2022, which can be accessed at <https://doi.org/10.1093/mnras/stac3664>.

SPECTRAL ANALYSIS

5.2 SWIFT/XRT Spectra of Mrk 739

Please note that SWIFT cannot resolve the two AGN present in Mrk739.

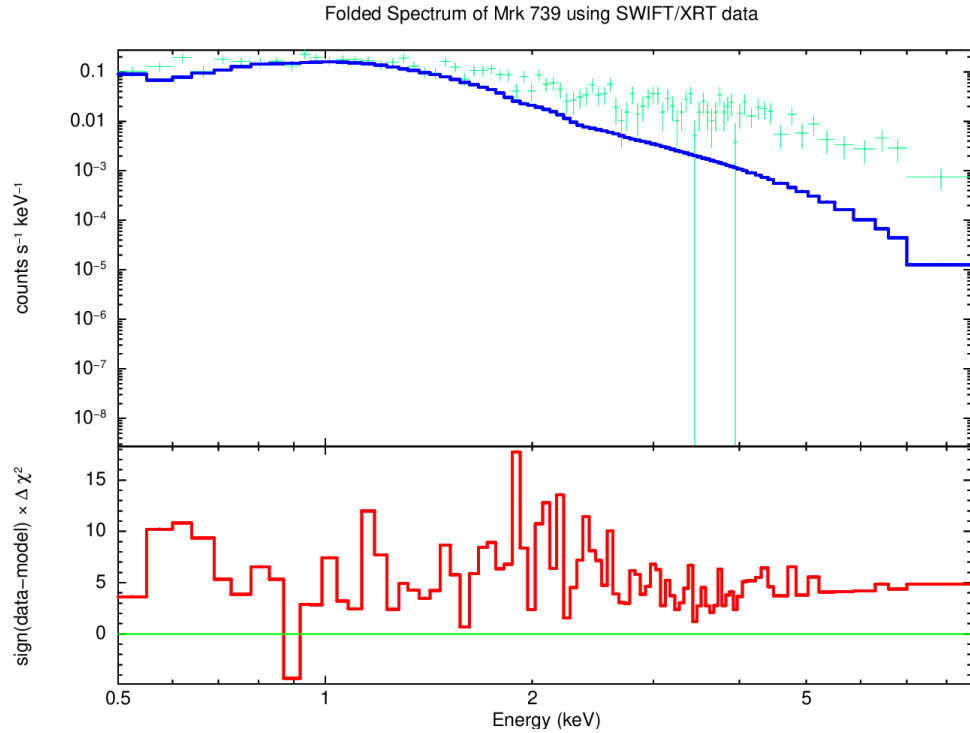


Figure 28: SWIFT/XRT Obs ID: 00037134001. Observed on date 2007-07-20 with XRT exposure of $\approx 4\text{ks}$

In spectral analysis, we used `ztbabs` and `zpow` models on an initially variable spectrum with large error bars. To improve statistical robustness, we rebinned energy channels into groups of 10, which streamlined the data and enhanced model accuracy. Despite these efforts, discrepancies remain, indicating potential needs for advanced modeling or further investigation, though these models are currently the best fit given the data and timeframe.²⁴

²⁴Blue-Model Fitting Line, Green - Error Bars, Red - ($\Delta\chi^2$)

Below we present SWIFT/XRT spectra of other two SWIFT/XRT observations of Mrk 739:

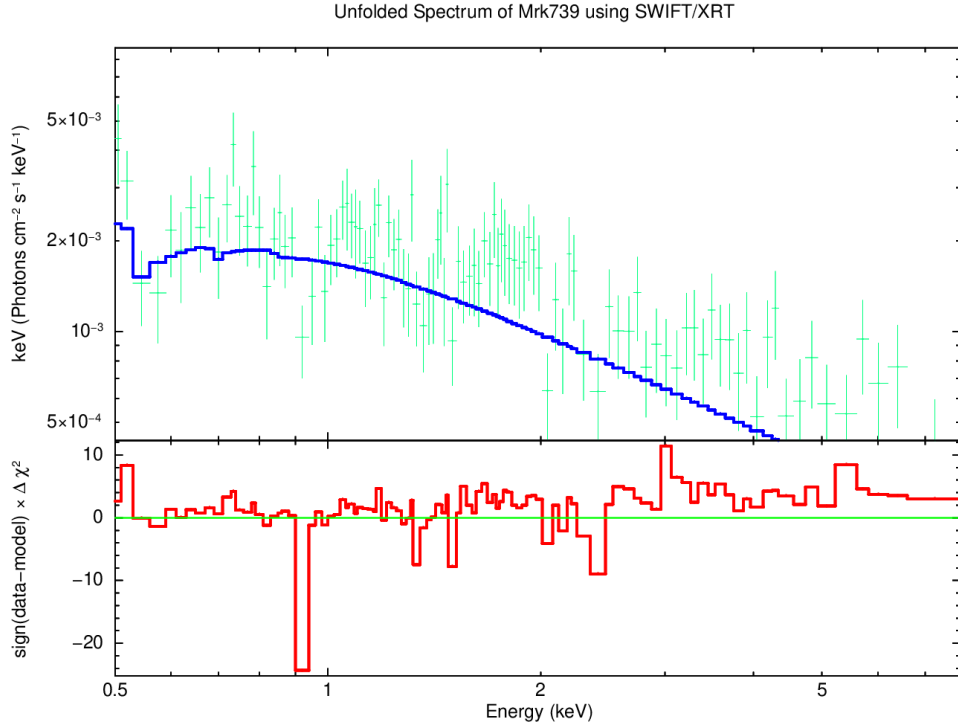


Figure 29: SWIFT/XRT Obs ID: 00037134002. Observed on date 2015-10-14 with XRT exposure of $\approx 8\text{ks}$

In our spectral analysis, we applied a consistent methodology as in previous investigations.²⁵ The notable dip observed at 1 keV emerged as a prominent feature consistently present across multiple observations of Mrk739. Other than the dip, low $\Delta\chi^2$ variations represents the optimal fit achievable within the constraints of the observation timeframe.

²⁵Blue - Model Fitting Line, Green - Error Bars, Red - ($\Delta\chi^2$)

The following is the spectral data obtained from the third and final observation of SWIFT/XRT targeting Mrk 739.

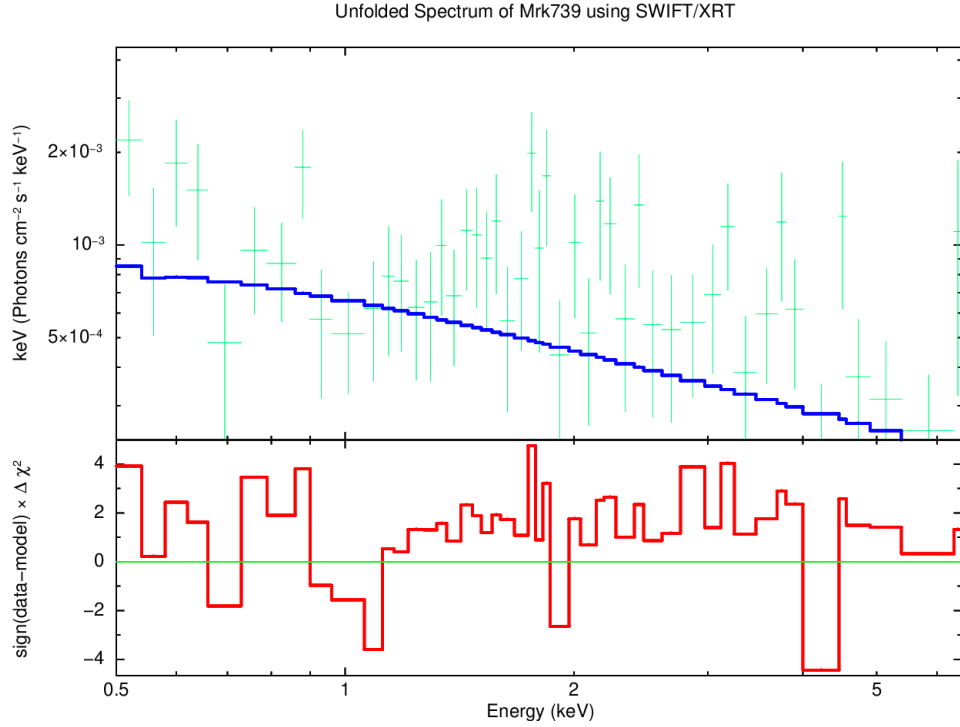


Figure 30: SWIFT/XRT Obs ID: 00081813001. Observed on date 2017-03-16 with XRT exposure of $\approx 2\text{ks}$

This observation had the shortest exposure, leading to a lower count rate and S/N ratio. Rebinning improved this, enabling successful spectral fitting with ztbabs and zpow models; the observation's $\delta\chi^2$ was small.²⁶

Spectra from all SWIFT/XRT observations of Mrk 739 were analyzed. Although SWIFT can't resolve Mrk 739's dual AGN components, its spectral analysis significantly contributes to understanding their combined emission.

²⁶Blue - Model Fitting Line, Green - Error Bars, Red - ($\Delta\chi^2$)

The following table shows the best fit parameters:

Table 5: Observation IDs and Spectral Parameters

| Obs ID | nH (10^{22}) | PhoInd | PowNorm | Flux (ergs/cm 2 /s) | χ^2 | Degrees of Free- dom |
|-------------|---------------------------------------|------------------------|--|--------------------------------------|----------|----------------------------|
| 00037134001 | $0.489790 \pm 6.36794 \times 10^{-2}$ | 4.41829 ± 0.295080 | 9.24042×10^{-3} 1.78228×10^{-3} | \times 8.95×10^{-13} | 478.94 | 424 |
| 00037134002 | $0.109500 \pm 3.26058 \times 10^{-2}$ | 2.10018 ± 0.112525 | 2.33658×10^{-3} 2.46376×10^{-4} | \times 4.83×10^{-12} | 305.93 | 396 |
| 00081813001 | 3.34493×10^{-2} | 1.64439 ± 0.238323 | 7.51447×10^{-4} 8.17479×10^{-2} | \times 1.90508×10^{-4} | 94.81 | 187 |

nH: Hydrogen column density **PhoInd:** Photon index **Pow Norm:** Normalization of the power-law model **LineE:** Energy of the spectral line **DoF:** Degrees of Freedom **χ^2 :** Chi-squared

1. Obs. 00037134001: 2007-07-20 04:21:01, MJD: 54301.18126
2. Obs. 00037134002: 2008-07-11 23:24:01, MJD: 54658.97501
3. Obs. 00081813001: 2017-03-16 05:18:56, MJD: 57828.22148

Spectral analysis reveals variability across observations. Obs. 00037134001 shows high absorption ($nH = 4.9 \times 10^{21} \text{ cm}^{-2}$) and a steep photon index ($PhoInd = 4.42$), indicating a soft spectrum. Obs. 00037134002 has lower absorption ($nH = 1.1 \times 10^{21} \text{ cm}^{-2}$) and a less steep photon index ($PhoInd = 2.10$), typical of AGN. Obs. 00081813001, with the least absorption ($nH = 0.3 \times 10^{21} \text{ cm}^{-2}$) and a harder photon index ($PhoInd = 1.64$), suggests different source characteristics. The χ^2 and DoF validate model fits, highlighting spectral diversity and the significance of model selection.

5.3 SWIFT/BAT Spectra of Mrk739

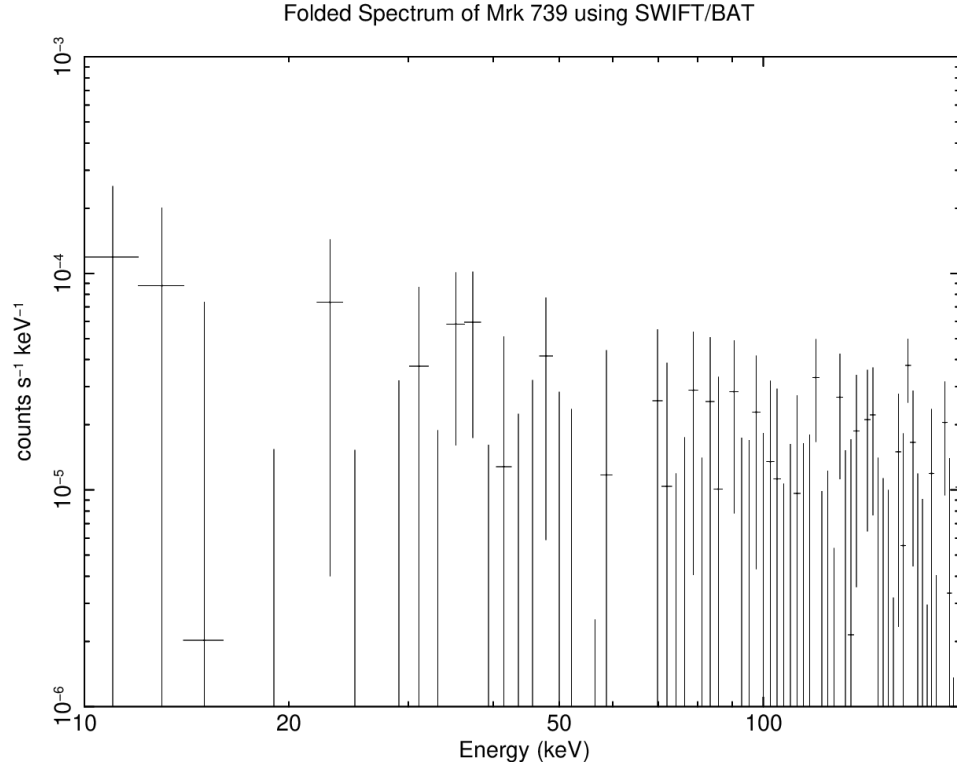


Figure 31: SWIFT/BAT Spectrum of Obs ID: 00037134002. Observed on date 2008-07-11 with BAT exposure of $\approx 8\text{ks}$

The spectrum above exhibits pronounced variability, rendering it challenging to fit any model accurately to the BAT spectrum. Nonetheless, this observation provides valuable insights into the source's behavior above 50keV , although conclusive findings remain elusive. Consequently, SWIFT/BAT spectral analysis may not significantly contribute to the study of the source Mrk739, particularly given the low S/N observed in this data.

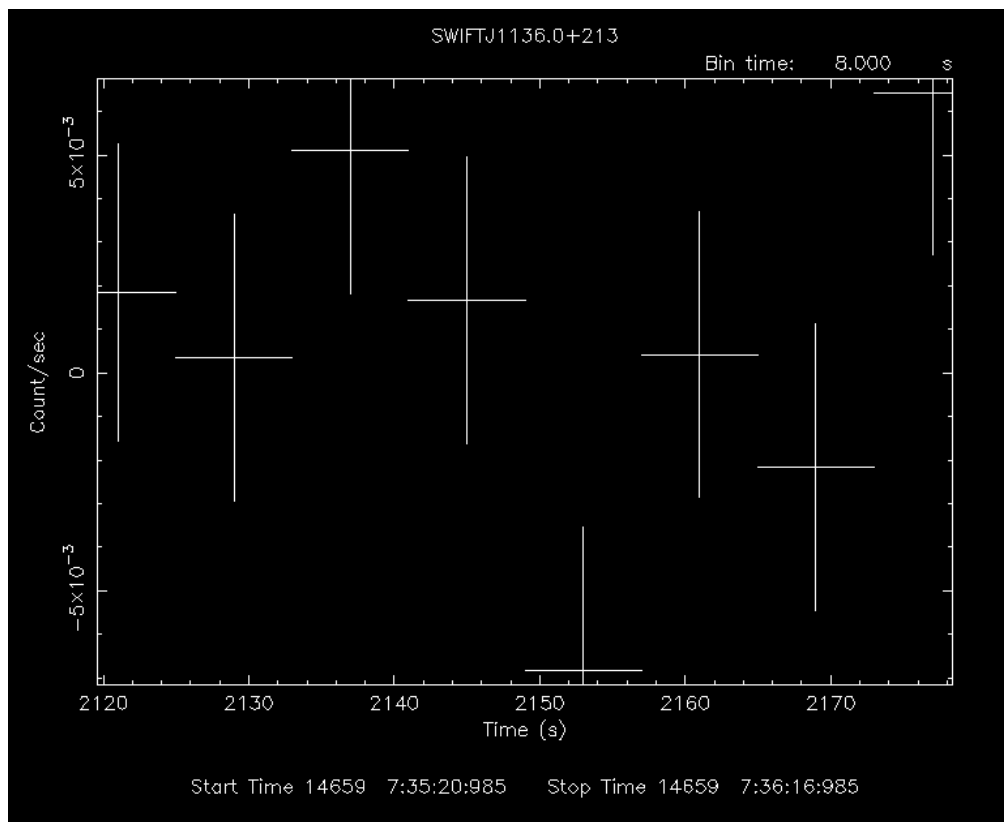


Figure 32: SWIFT/BAT Lightcurve of Obs ID: 00037134002. Observed on date 2008-07-11 with BAT exposure of $\approx 8\text{ks}$

Here we present the SWIFT/BAT lightcurve, providing insights into the timing analysis of the SWIFT/BAT observation. The bin time of the lightcurve is 8.0.

5.4 NuSTAR Spectra of Mrk 739

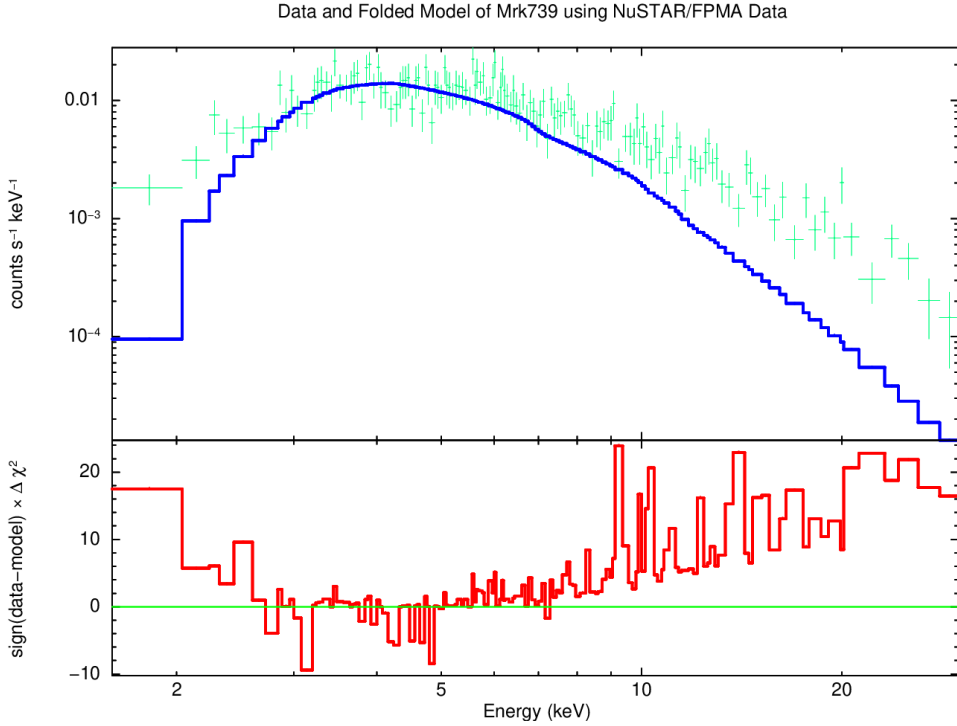


Figure 33: NuSTAR/FPMA Spectrum Obs ID: 60260008002. Observed on date 2017-03-16 with the exposure of $\approx 18\text{ks}$

In the spectral fitting process, we employed the `ztbabs` and `zpowerlaw` models. Since the initial spectrum had large error bars above 15 keV, we rebinned the data by grouping adjacent energy channels in sets of 15. This helped us to obtain a more refined spectrum and hence improved the accuracy of model fitting. $\Delta \chi^2$ is high for this spectrum, which is mostly due to high variability in the spectrum above 9 keV. However, more advanced models need to be utilized to fit the spectrum even better. Within the given timeframe, however, the models employed represent the best fit for the available data.²⁷

²⁷Blue - Model Fitting Line, Green - Error Bars, Red - ($\Delta \chi^2$).

Below are the comparative simultaneous spectra obtained from NuSTAR's FPMA and FPMB modes:

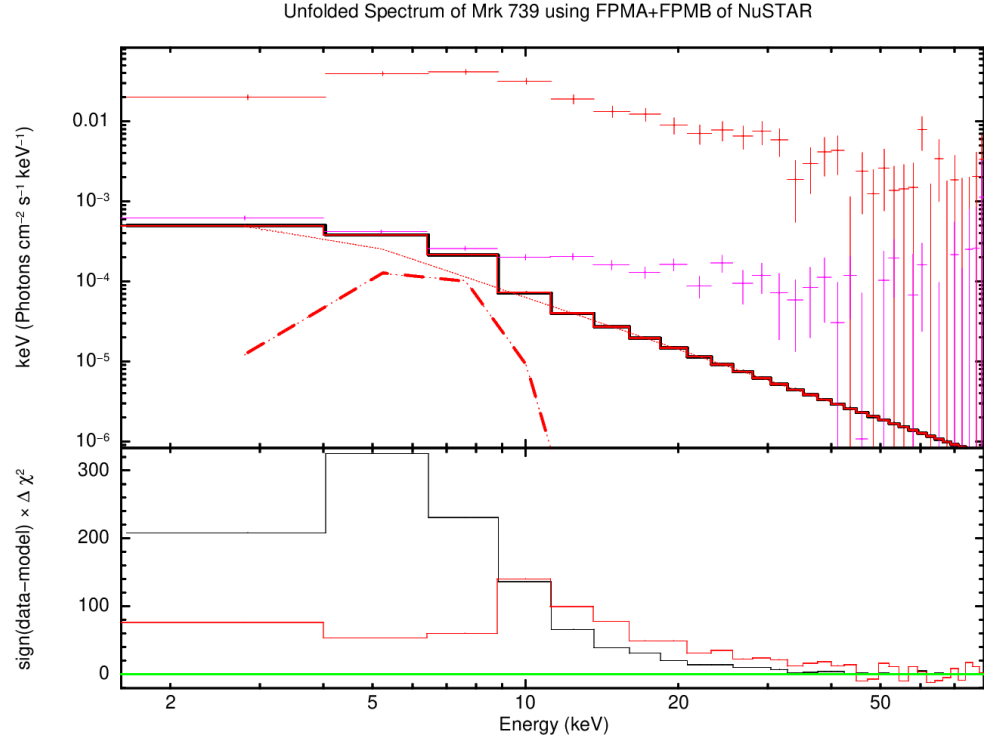


Figure 34: Simultaneous Spectra of NuSTAR's FPMA and FPMB Modes. Obs ID: 60260008002. Observed on date 2017-03-16 with the exposure of $\approx 18\text{ks}$

Orange - FPMA Spectrum, Purple - FPMB Spectrum

As evident from the simultaneous plot of NuSTAR/FPMA and NuSTAR/FPMB above, NuSTAR/FPMA exhibits a significantly higher count rate compared to NuSTAR/FPMB. Consequently, we excluded the NuSTAR/FPMB spectrum from our analysis. Combining both spectra compromises the quality of the spectral features; refer Figure 34.

Table 6: Spectral Parameters of 60260008002

| Source Name | nH (10^{22}) | PhoInd | PowNorm | Flux (ergs/cm 2 /s) | χ^2 | Degrees of Freedom |
|-------------|--------------------|------------------------------------|--|---------------------------|----------------------------------|--------------------|
| 60260008002 | 9.80848 1.42974 | \pm 3.51771 \pm 0.145839 | 3.54213 10^{-2} 1.09421×10^{-2} | \times \pm | 3.65×10^{-12} 746.07 | 706 |

nH: Hydrogen column density **PhoInd:** Photon index **Pow Norm:** Normalization of the power-law model **LineE:**

Energy of the spectral line **DoF:** Degrees of Freedom **χ^2 :** Chi-squared

Obs. 60260008002: 2017-03-16 3:56:09, MJD: 57828.16399

Source 60260008002 exhibits high absorption ($nH = 9.8 \times 10^{22} \text{ cm}^{-2}$) and a steep photon index ($PhoInd = 3.52$), indicative of dense media or intense accretion. Its significant power-law normalization ($PowNorm = 3.5 \times 10^{-2}$) and flux ($3.65 \times 10^{-12} \text{ ergs/cm}^2/\text{s}$) point to a luminous source. A χ^2 of 746.07 for 706 DoF suggests a reasonable model fit, with room for minor adjustments to enhance accuracy.

5.5 XMM-Newton Spectra of Mrk 739

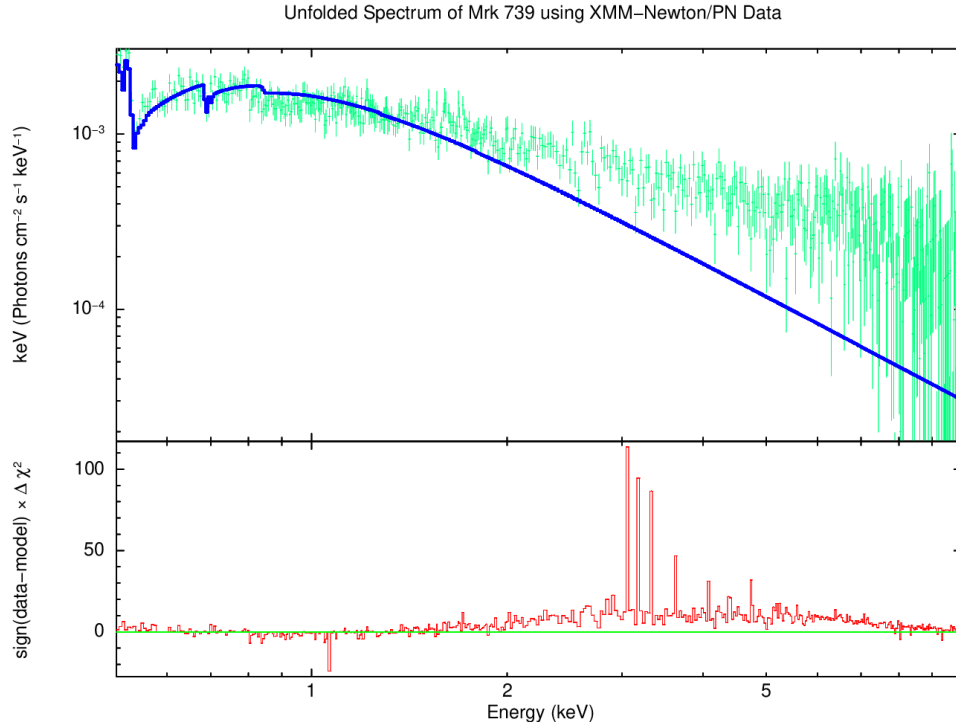


Figure 35: XMM-Newton/PN Spectrum Obs ID: 0601780401. Observed on date 2009-06-14 with the exposure of $\approx 12\text{ks}$

The XMM-Newton/PN spectrum of Mrk 739 analysis using `ztbabs` and `zpow` models showed good fit between 500 eV and 2000 eV but variability at 3 keV to 4 keV. Despite rebinning to enhance S/N, further adjustments risked losing critical features. Given the data and time constraints, these models best represent Mrk 739's spectrum.²⁸

²⁸Blue - Model Fitting Line, Green - Error Bars, Purple - $(\Delta \chi^2)$

Table 7: Spectral Parameters of 601780401

| Obs ID | nH (10^{22}) | PhoInd | PowNorm | Flux (ergs/cm 2 /s) | χ^2 | Degrees of Free- dom |
|------------|-------------------------------------|------------------------------------|---------|---------------------------|----------|----------------------------|
| 0601780401 | 0.216608 ± 8.22620×10^{-3} | 2.91651 ± 3.40561×10^{-2} | 2.97801 | × 1.90×10^{-12} | 2408.42 | 1301 |

nH: Hydrogen column density **PhoInd:** Photon index **Pow Norm:** Normalization of the power-law model **LineE:** Energy of the spectral line **DoF:** Degrees of Freedom χ^2 : Chi-squared

Obs. 060178041: 2009-06-14 8:23:45, MJD: 54996.34983

Mrk739's XMM-Newton/PN data (Obs ID 0601780401) analysis reveals a moderate hydrogen column density ($nH = 2.2 \times 10^{21} \text{ cm}^{-2}$), suggesting light absorption. A steep photon index ($PhoInd = 2.92$) is typical of sources with significant soft X-ray output, hinting at an AGN. Despite a strong emission signal, a high χ^2 value of 2408.42 against 1301 DoF indicates the model captures the trend but may miss some complexities, suggesting further refinement or additional components might be necessary.

5.6 Chandra/ACIS-S Observation of Mrk 739

Unlike SWIFT, XMM-Newton, and NuSTAR, Chandra is known for its high-resolution X-ray observations covering the energy range from 200 eV to 10,000 eV. This distinct capability makes Chandra the only X-ray telescope capable of resolving closely separated dual active galactic nuclei (AGN). Utilizing this unique feature, we acquired individual spectra for both AGN components, Mrk 739E and Mrk 739W, enabling a thorough examination of each AGN separately and allowing for a comparative analysis with the combined spectrum results.

SPECTRUM OF MRK 739E

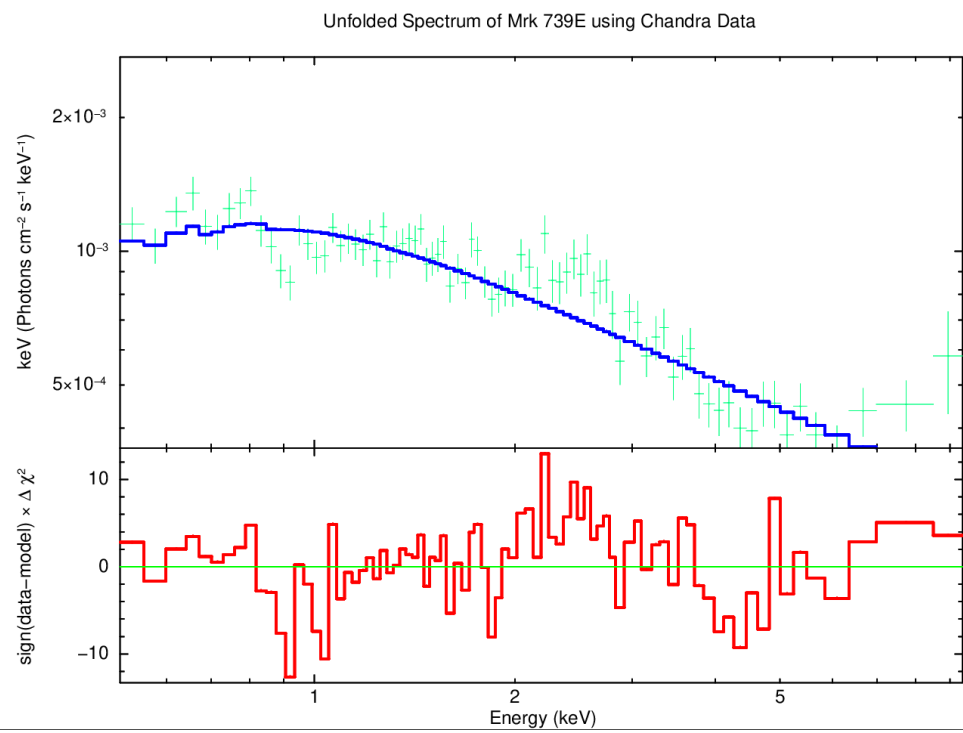


Figure 36: Chandra/ACIS-S Spectrum of Mrk 739W, Obs ID: 12863. Observed on date 2011-04-22 with the exposure of $\approx 13\text{ks}$

Above spectrum represents the Chandra spectrum of Mrk 739E.²⁹ To address variability in the spectrum, we re-binned it by combining adjacent energy channels in sets of 5, resulting in an improved representation of spectral features. Our analysis utilized the tbabs and zpowerlaw models for optimal fitting. Fluctuations observed in $\Delta\chi^2$ within the range of -10 to 5 suggest a satisfactory fit.

²⁹Blue - Model Fitting Line, Green - Error Bars, Red - ($\Delta\chi^2$)

SPECTRUM OF MRK 739W

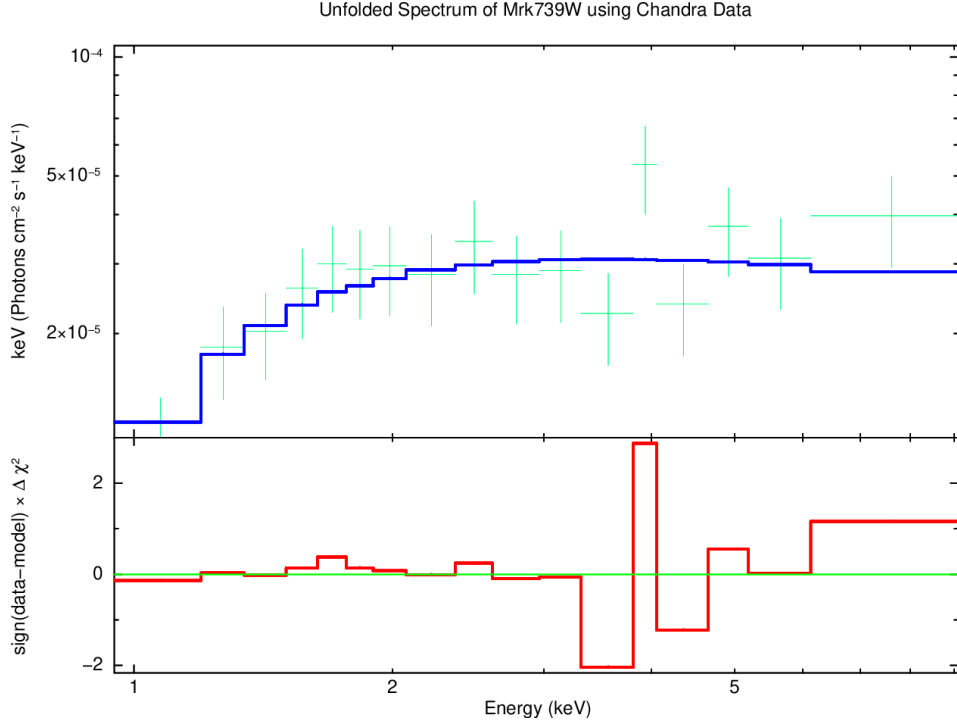


Figure 37: Chandra/ACIS-S Spectrum of Mrk 739W, Obs ID: 12863. Observed on date 2011-04-22 with the exposure of $\approx 13\text{ks}$

The data from Mrk 739W exhibited low counts, rendering it challenging to discern specific spectral features conclusively. Despite employing the tbabs and zpowerlaw models, the spectrum indicated an uncertain fit between 3keV to 5keV³⁰. However, due to the limited number of counts, drawing definitive conclusions from this fitting is not advisable. Nevertheless, we present the best-fit parameters in Table 8.

³⁰Blue - Model Fitting Line, Green - Error Bars, Red - ($\Delta\chi^2$)

COMBINED SPECTRUM OF MRK 739E AND MRK 739W

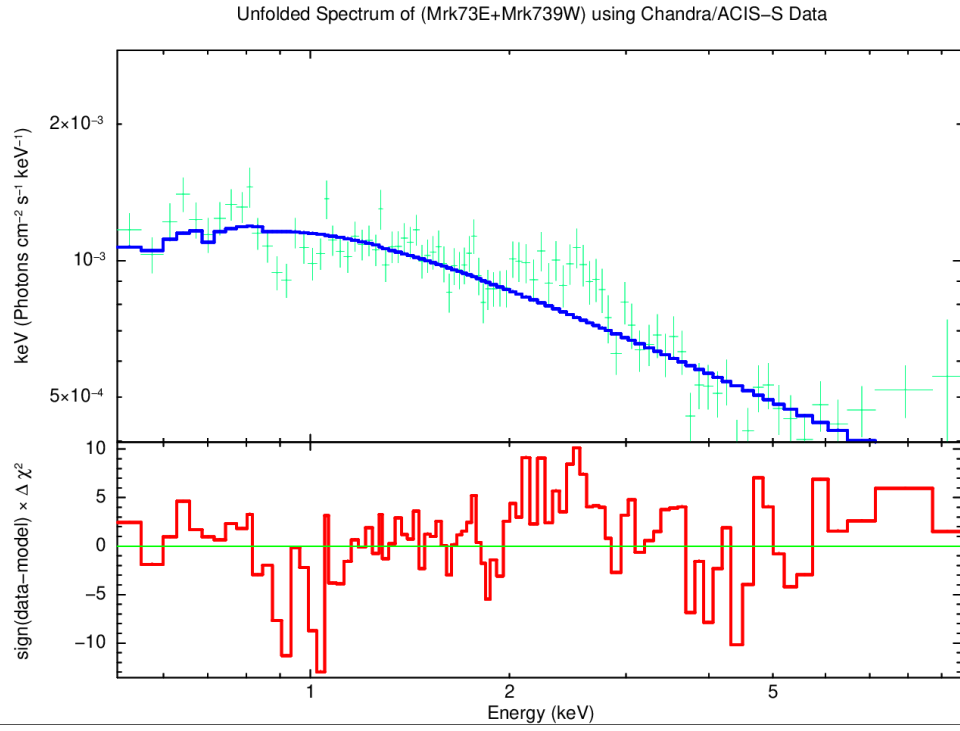


Figure 38: Chandra/ACIS-S Spectrum of Mrk 739W, Obs ID: 12863. Observed on date 2011-04-22 with the exposure of $\approx 13\text{ks}$

In the combined spectrum³¹ of Mrk 739E and Mrk 739W, it is evident that the spectral characteristics closely resemble those of Mrk 739E. This disparity can be attributed to the higher count rate of Mrk 739E, which dominates over Mrk 739W with its lower count rate. Nevertheless, notable differences are observed, particularly above 5 keV. Despite these variations, the fit appears to be satisfactory, as indicated by the minimal fluctuations in $\Delta\chi^2$.

³¹Blue - Model Fitting Line, Green - Error Bars, Red - ($\Delta\chi^2$)

Table 8: Spectral Parameters of Mrk739E, Mrk739W, and Combined

| Source | nH (10^{22}) | PhoInd | Pow Norm | Flux (ergs/cm 2 /s) | χ^2 | DoF | |
|------------------------------------|--|--------------------------------|---|---------------------------|--|--------|-----|
| Mrk739E | 8.13148 10^{-2} | \times \pm | $1.68851 \pm$ 3.04744×10^{-3} | 1.40810 \pm | 5.53×10^{-12} | 306.47 | 252 |
| | 1.04019×10^{-2} | 10^{-2} | 4.43636×10^{-5} | | | | |
| Mrk739W | 0.587926 0.241006 | \pm | $1.14677 \pm$ 0.250725 | 4.04963 10^{-5} | 3.77×10^{-13} 1.40136×10^{-5} | 9.2 | 14 |
| Mrk739E + Mrk739W (Combined) | 8.08423 10^{-2} 1.01913×10^{-2} | \times \pm 10^{-2} | $1.64933 \pm$ 2.94434×10^{-3} | 1.46149 \pm | 6.11×10^{-12} 4.49053×10^{-5} | 308.9 | 258 |

nH: Hydrogen column density **PhoInd:** Photon index **Pow Norm:** Normalization of the power-law model **LineE:**

Energy of the spectral line **DoF:** Degrees of Freedom χ^2 : Chi-squared

This observation was taken on 2011-04-22 02:26:55, MJD: 55673.10202546 The spectral parameters of Mrk739E, Mrk739W, and their combined spectrum are summarized in Table 8.

The spectral analysis differentiates Mrk739E, Mrk739W, and their combined spectra. Mrk739W, with higher nH and a flatter spectral energy distribution (*PhoInd*), implies more obscuration or a denser medium than Mrk739E, whose characteristics dominate the combined data. This hints at varied accretion processes or environments. Goodness of fit metrics (χ^2 and DoF) indicate a reasonable match for Mrk739E and the combined data, with a better fit for the simpler spectrum of Mrk739W, showcasing the spectral diversity and environmental distinctions between the two.

Below, we present simultaneous plots of Mrk 739E, Mrk 739W, and the combined Mrk 739. Red

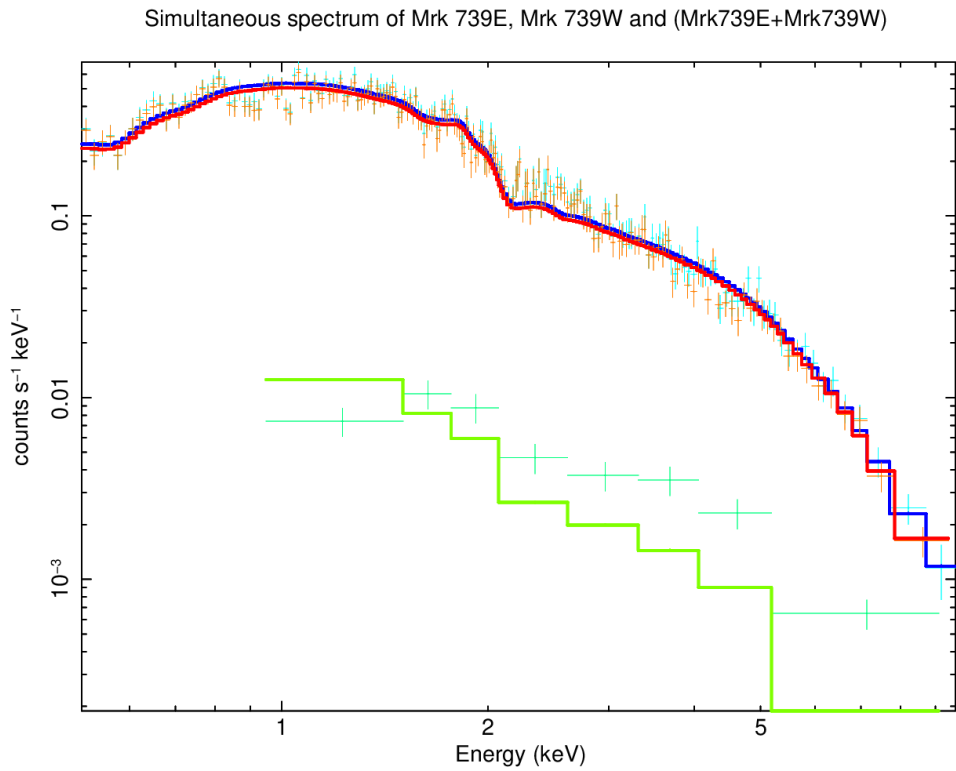


Figure 39: Simultaneous Folded Spectrum of Mrk739E, Mrk739W and (Mrk739E+Mrk739W)

- Model Fit of Mrk739E, Orange - Error Bars of Mrk 739E, Green - Model Fit of Mrk739W, Cyan - Error Bars of Mrk739W, Blue - Model Fit of (Mrk739E+Mrk739W), LightBlue - Error Bars of (Mrk739E+Mrk739W).

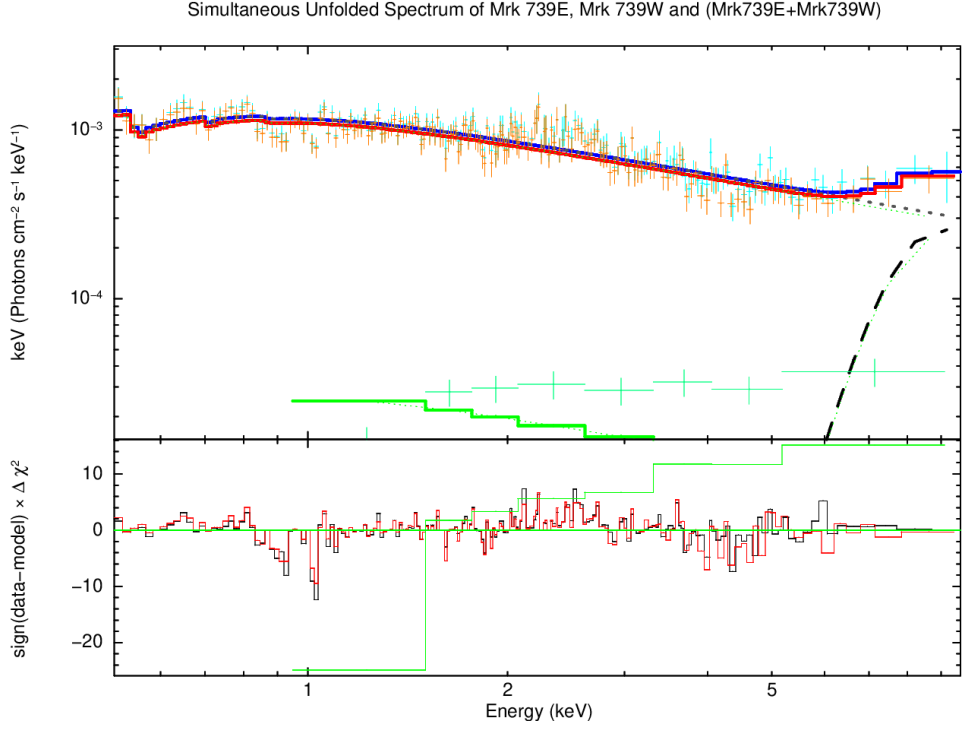


Figure 40: Simultaneous Unfolded Spectrum of Mrk739E, Mrk739W and (Mrk739E+Mrk739W)

The simultaneous analysis of the unfolded spectrum for the dual AGN Mrk 739, using Chandra data, reveals distinct contributions from Mrk 739E and Mrk 739W. Specifically, Mrk 739E significantly overshadows Mrk 739W in the combined spectrum, with a count rate more than tenfold higher. The $\Delta\chi^2$ analysis shows minor fluctuations for Mrk 739E and the combined spectrum, contrasted by notable fluctuations for Mrk 739W. This comprehensive comparison underscores the unique spectral characteristics and contributions of each AGN within the Mrk 739 system.

Below we present the simultaneous plot of spectra NuSTAR/FPMA, SWIFT/XRT, XMM-Newton/PN, SWIFT/BAT and Chandra/ACIS-S for Mrk739.

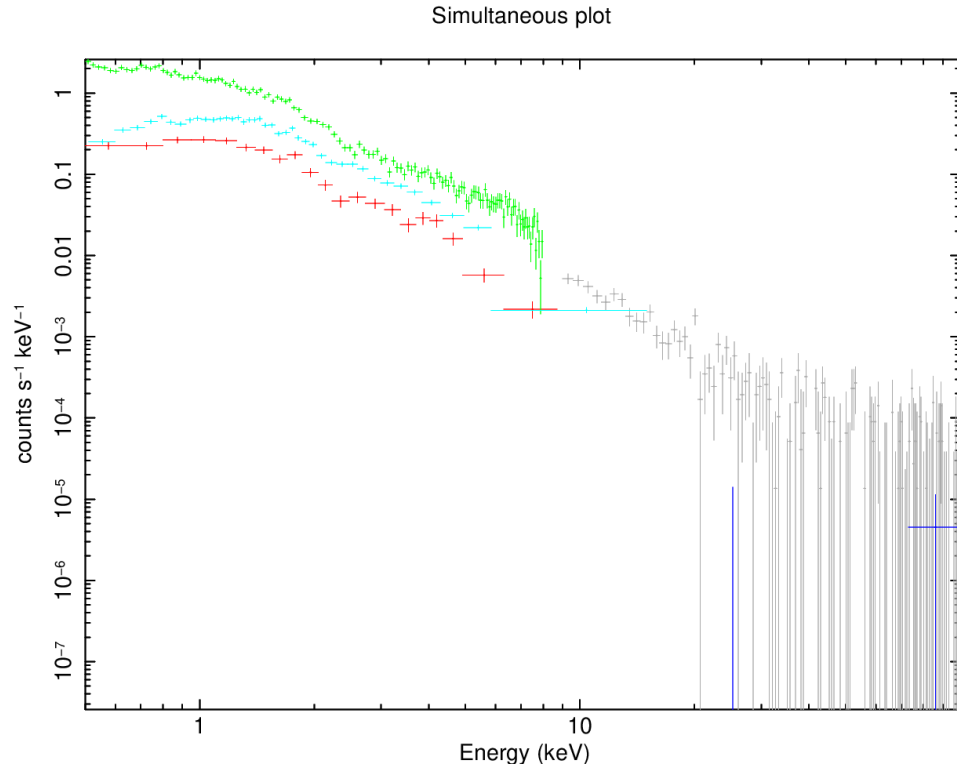


Figure 41: Simultaneous Unfolded Spectrum of Mrk739E, Mrk739W and (Mrk739E+Mrk739W)

Green - XMM-Newton, Red - SWIFT/XRT, LightBlue - Chandra/ACIS-S, Grey - NuSTAR/FPMA,
 Blue - SWIFT/BAT

In the simultaneous spectra analysis, we rebinned 15 adjacent energy channels, providing clearer comparative insights and broader energy coverage. This technique simplifies analysis and enriches our understanding of spectral characteristics across observations.

CHAPTER 6: CONCLUSIONS AND FUTURE SCOPE

6.1 Conclusion

In conclusion, we have conducted image and spectral analysis of the dual AGN, Mrk 739. During this process, we determined the projected nuclear separation of Mrk 739 and other dual AGN sources, as shown in Table 4. Additionally, we identified potential candidate dual AGN. The superior resolution of the Chandra Space Telescope over other X-ray telescopes was demonstrated in this study. Through image analysis, we took the first step towards identifying dual AGN in the X-ray and High Energy Regime.

Subsequently, with the aid of spectral analysis, we investigated the spectra of the dual AGN Mrk 739. We employed spectral models commonly used for AGN and observed variations in the fit, suggesting that dual AGN may exhibit significantly different spectral features than single AGN. The $\Delta\chi^2$ dip observed in Mrk739E (see Fig. 21) and the composite Mrk739 (see Fig. 38) most notably deviated from the powerlaw model. Moreover, we presented the flux measurements for all observations.

We compared the individual spectra of Mrk739E and Mrk739W with the composite spectra of dual AGN Mrk739 to gain insights into their comparative study. However, given the data quality and the limited timeframe, no definitive conclusions could be drawn.

Furthermore, we plotted the simultaneous spectra of all data from observatories SWIFT/XRT, SWIFT/BAT, NuSTAR/FPMA, XMM-Newton/PN, and Chandra/ACIS-S, providing insights into the count rate of the observations.

6.2 Future Scope

1. The significant dip in the spectra of Mrk739 at around 1 keV warrants further study using advanced modeling techniques and additional follow-up observations.
2. Results can be compared with confirmed Binary AGN such as NGC 6240 to conduct a comparative analysis and identify X-ray spectral characteristics indicative of Binary AGN.
3. The methodology employed here can be used to uncover more dual AGN candidates.

APPENDIX-A

In this section, we provide supplementary images obtained through the course of this thesis research.

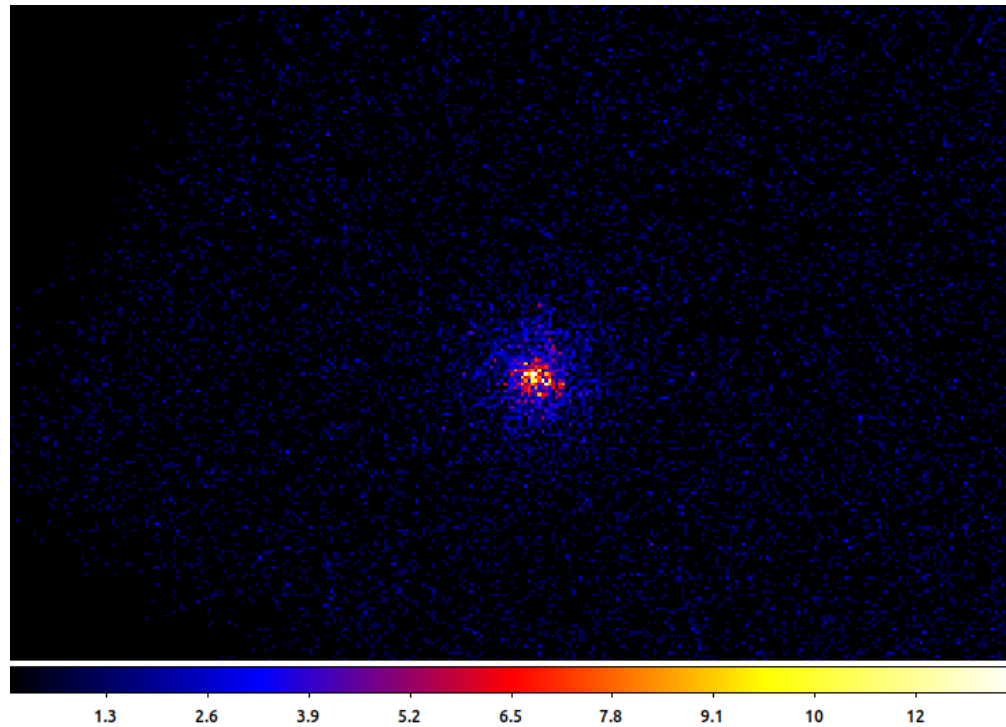


Figure 42: NuSTAR Image of Mrk 739

NuSTAR, with its limited resolution, is unable to distinguish between the two AGN within the dual AGN system Mrk 739.

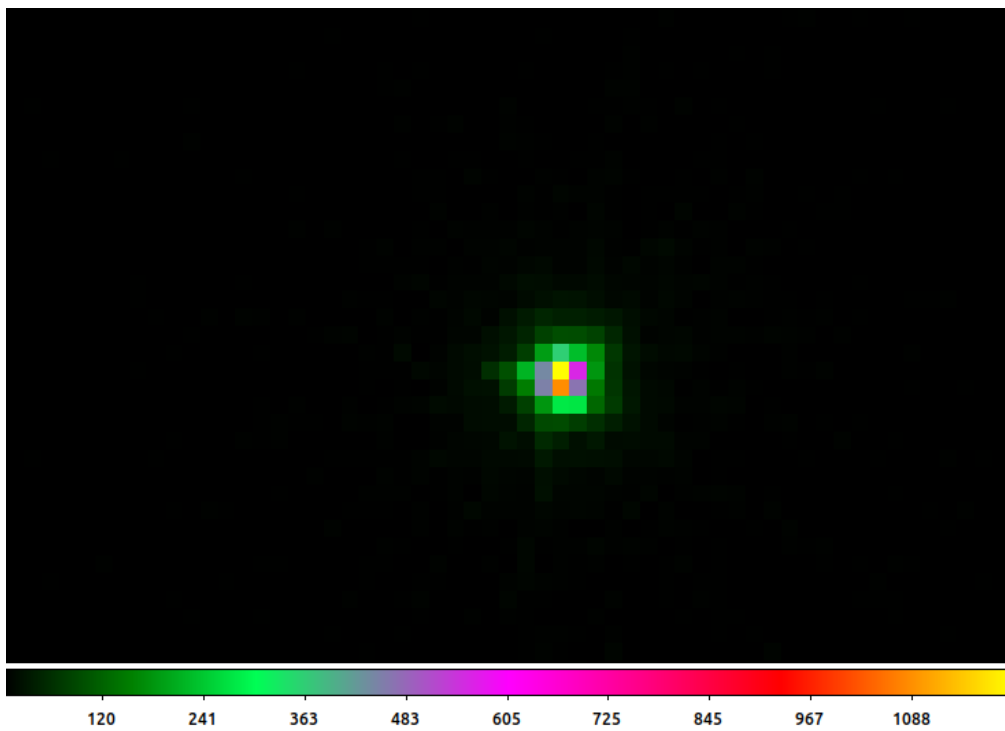
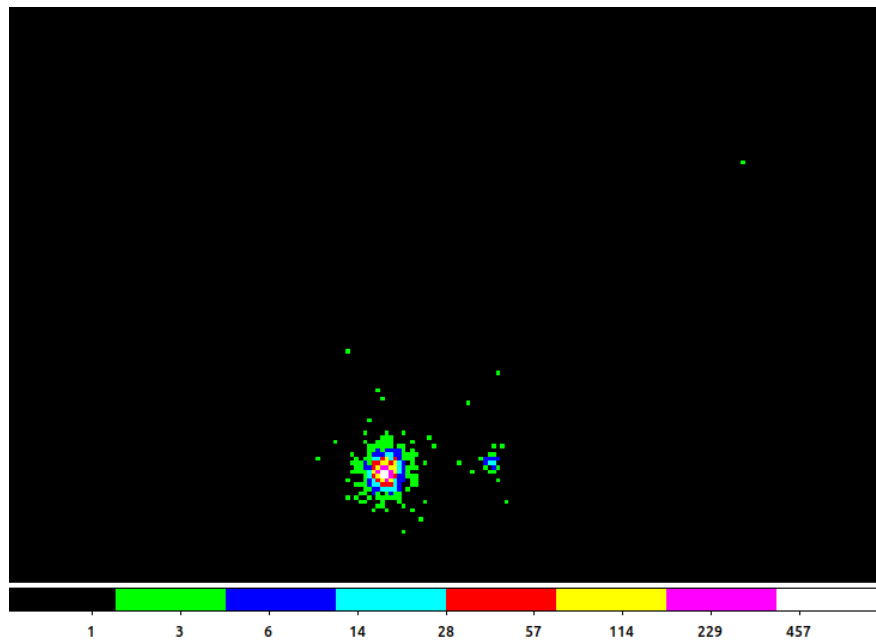
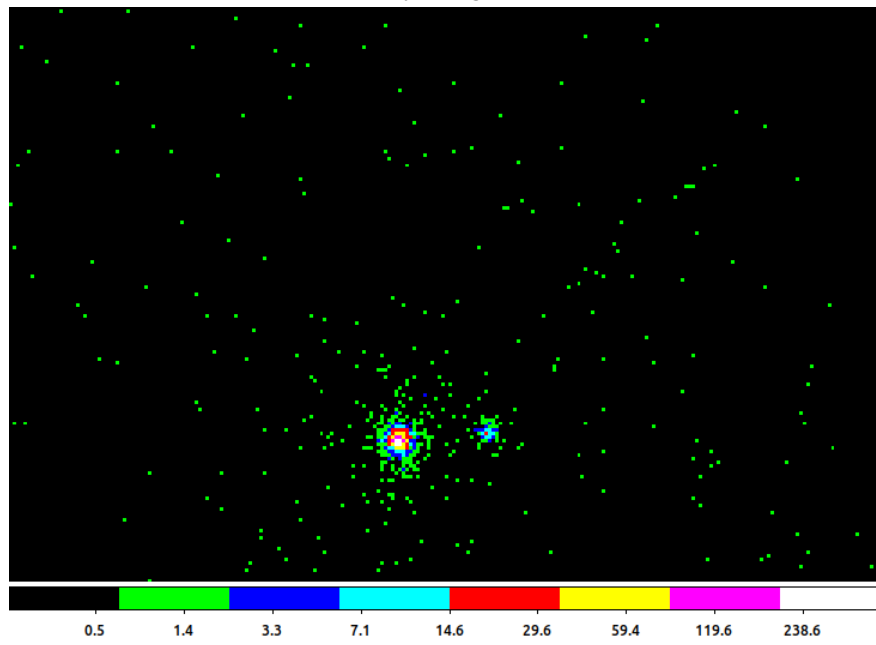


Figure 43: XMM-Newton/EPIC X-ray Image of Mrk 739

The XMM-Newton/OM successfully resolved two AGN within the dual AGN system Mrk 739 by observing in the optical and UV ranges (refer Fig. 19). However, XMM-Newton/EPIC was unable to resolve the two AGN, as it operates in the X-ray band.



(a) Soft X-ray Image of Mrk 739



(b) Hard X-ray Image of Mrk 739

Figure 44: Comparison of Soft and Hard X-ray Images of Mrk 739

APPENDIX-B

Here we provide supplementary spectra obtained through the course of this thesis research.

BINARY AGN NGC 6240

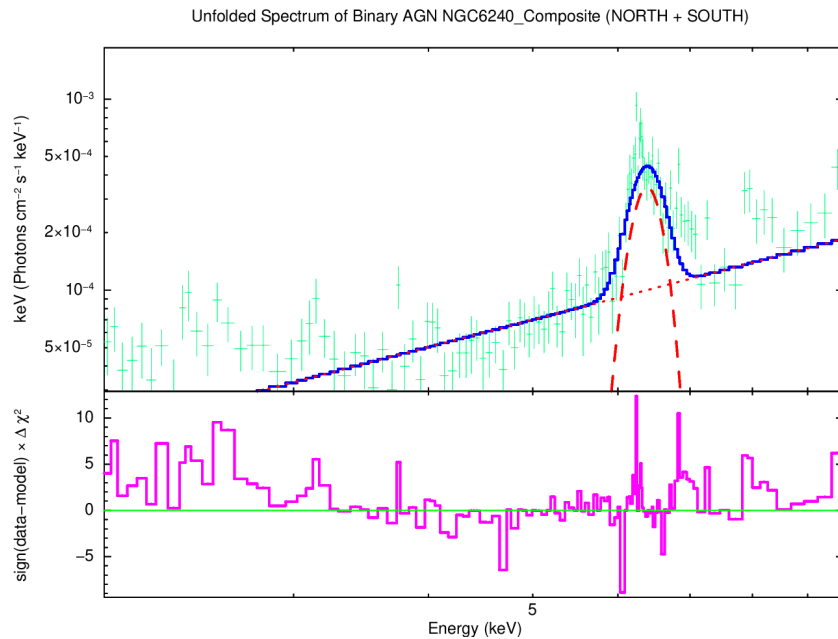
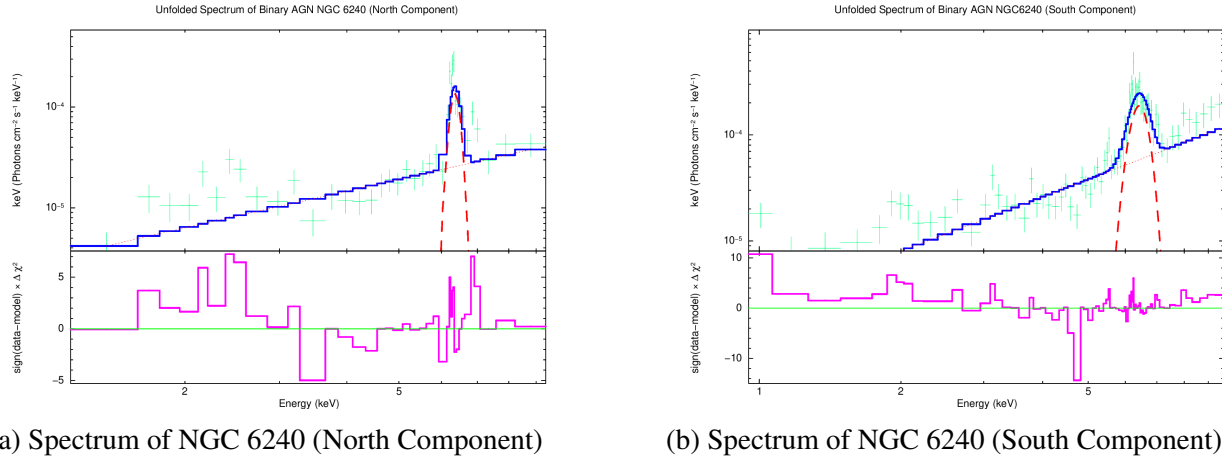


Figure 46: Spectrum of NGC 6240 Composite (North + South)

DUAL AGN Mrk 463

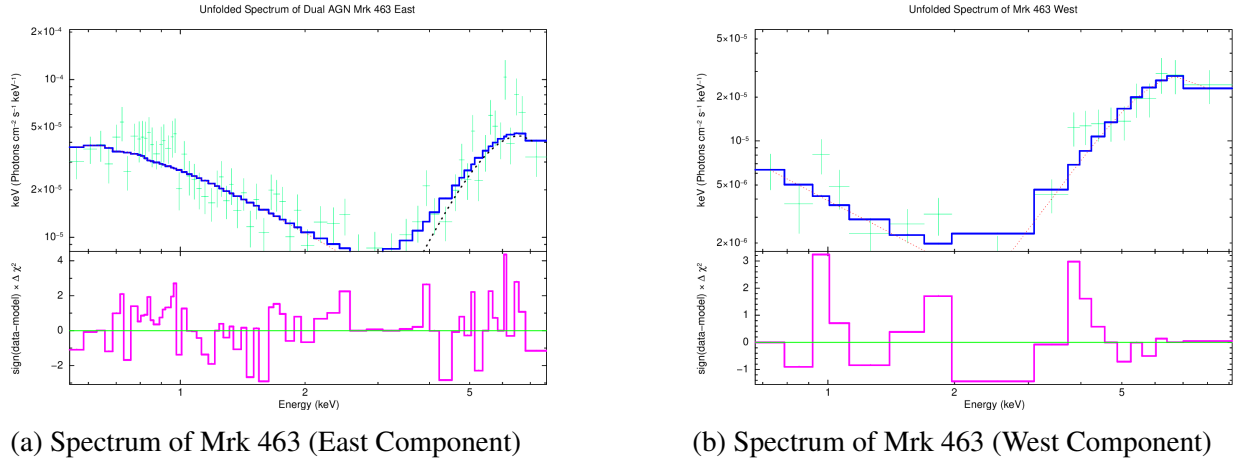


Figure 47: Spectra of Mrk 463 (East and West Components)

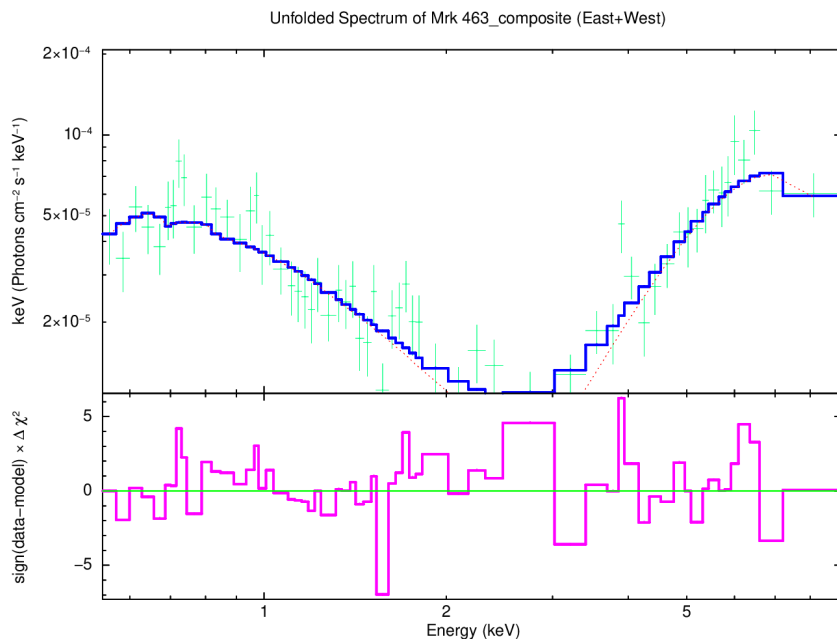


Figure 48: Spectrum of Mrk 463 Composite (East + West)

References

- Armitage, P. J., & Natarajan, P. (2002). Accretion during the merger of supermassive black holes. *The Astrophysical Journal Letters*, 567, L9–L12. <https://doi.org/10.1086/339770>
- Barthelmy, S. D., et al. (2005). The burst alert telescope (bat) on the swift midex mission. *Space Science Reviews*, 120, 143–164. <https://doi.org/10.1007/s11214-005-5096-3>
- Begelman, M. C., Blandford, R. D., & Rees, M. J. (1980). Massive black hole binaries in active galactic nuclei. *Nature*, 287, 307–309. <https://doi.org/10.1038/287307a0>
- Begelman, M. C., Volonteri, M., & Rees, M. J. (2006). Formation of supermassive black holes by direct collapse in pre-galactic haloes. *Monthly Notices of the Royal Astronomical Society*, 370, 289–298. <https://doi.org/10.1111/j.1365-2966.2006.10467.x>
- Berczik, P., Merritt, D., Spurzem, R., & Bischof, H.-P. (2006). Efficient merger of binary supermassive black holes in nonaxisymmetric galaxies. *The Astrophysical Journal Letters*, 642, L21. <https://doi.org/10.1086/504842>
- Bhattacharya, A., Nehal, C. P., Das, M., Paswan, A., Saha, S., & Combes, F. (2023). Automated detection of double nuclei galaxies using Gothic and the discovery of a large sample of dual AGN. *Monthly Notices of the Royal Astronomical Society*, 524(3), 4482–4497. <https://doi.org/10.1093/mnras/stad2117>
- Bonetti, M., Sesana, A., Haardt, F., Barausse, E., & Colpi, M. (2018). Post-newtonian evolution of massive black hole triplets in galactic nuclei: I. numerical implementation and tests. *Monthly Notices of the Royal Astronomical Society*, 477, 3910–3927. <https://doi.org/10.1093/mnras/sty857>
- Bundy, K., Bershady, M. A., Law, D. R., Yan, R., Drory, N., MacDonald, N., Wake, D. A., Cherinka, B., Sánchez-Gallego, J. R., Weijmans, A.-M., Thomas, D., Tremonti, C., Masters, K., Coccato, L., Diamond-Stanic, A. M., Aragón-Salamanca, A., Avila-Reese, V., Badenes, C., Falcón-Barroso, J., ... Zhang, K. (2015). Overview of the sdss-iv manga survey: Mapping nearby galaxies at apache point observatory. *The Astrophysical Journal*, 798, 7. <https://doi.org/10.1088/0004-637X/798/1/7>
- Burke-Spolaor, S. (2014). Gravitational waves from binary supermassive black holes missing in pulsar observations. *Science*, 343, 53–56. <https://doi.org/10.1126/science.1248759>

- Burke-Spolaor, S., Taylor, S. R., Charisi, M., Dolch, T., Hazboun, J. S., Holgado, A. M., Kelley, L. Z., Lazio, T. J. W., Madison, D. R., McMann, N., Mingarelli, C. M. F., Rasskazov, A., Simon, J., Smith, T. L., & Vigeland, S. J. (2019). The astrophysics of nanohertz gravitational waves. *The Astronomy and Astrophysics Review*, 27, 5. <https://doi.org/10.1007/s00159-019-0115-7>
- Burrows, D. N., et al. (2005). The swift x-ray telescope. *Space Science Reviews*, 120, 165–195. <https://doi.org/10.1007/s11214-005-5097-2>
- Chandra proposers' observatory guide*. (2021). Chandra X-ray Center. <https://cxc.harvard.edu/proposer/POG/>
- Cuadra, J., Armitage, P. J., Alexander, R. D., & Begelman, M. C. (2008). Galactic centre star formation: The case of the missing gas disc. *Monthly Notices of the Royal Astronomical Society*, 393, 1423–1432. <https://doi.org/10.1111/j.1365-2966.2008.14147.x>
- Di Matteo, T., Springel, V., & Hernquist, L. (2005). Energy input from quasars regulates the growth and activity of black holes and their host galaxies. *Nature*, 433, 604–607. <https://doi.org/10.1038/nature03335>
- Dotti, M., Colpi, M., Haardt, F., & Mayer, L. (2007). Supermassive black hole binaries in gaseous and stellar circumnuclear disks: Orbital dynamics and gas accretion. *Monthly Notices of the Royal Astronomical Society*, 379, 956–962. <https://doi.org/10.1111/j.1365-2966.2007.11988.x>
- Escala, A., Larson, R. B., Coppi, P. S., & Mardones, D. (2005). The role of gas in the merging of massive black holes in galactic nuclei. i. black hole merger trees. *The Astrophysical Journal*, 630, 152–166. <https://doi.org/10.1086/431747>
- Fabian, A. C. (2012). Observational evidence of active galactic nuclei feedback. *Annual Review of Astronomy and Astrophysics*, 50, 455–489. <https://doi.org/10.1146/annurev-astro-081811-125521>
- Fan, X., Liao, K., Bao, M., Zhang, B., Li, S., & Bai, J. (2016). A survey of dual active nuclei in mergers: The prevalence of binary active galactic nuclei. *The Astrophysical Journal*, 822, L32. <https://doi.org/10.3847/2041-8205/822/1/L32>

- Ferrarese, L., & Merritt, D. (2000). A fundamental relation between supermassive black holes and their host galaxies. *The Astrophysical Journal*, 539, L9–L12. <https://doi.org/10.1086/312838>
- Foreman, G., Volonteri, M., & Dotti, M. (2009). Observations of feedback from radio-quiet quasars – ii. kinematics of ionized gas nebulae. *The Astrophysical Journal*, 693, 1554–1565. <https://doi.org/10.1088/0004-637X/693/2/1554>
- Fragos, T., Lehmer, B. D., Tremmel, M., Tzanavaris, P., Basu-Zych, A., Belczynski, K., Hornschemeier, A., Jenkins, L., Kalogera, V., Ptak, A., & Zezas, A. (2013). X-ray binary evolution across cosmic time. *The Astrophysical Journal Letters*, 776, L31. <https://doi.org/10.1088/2041-8205/776/2/L31>
- Gebhardt, K., et al. (2000). A relationship between nuclear black hole mass and galaxy velocity dispersion. *The Astrophysical Journal*, 539, L13–L16. <https://doi.org/10.1086/312840>
- Gehrels, N., et al. (2004). The swift gamma-ray burst mission. *The Astrophysical Journal*, 611(2), 1005–1020. <https://doi.org/10.1086/422091>
- Genzel, R., Eisenhauer, F., & Gillessen, S. (2010). The galactic center massive black hole and nuclear star cluster. *Reviews of Modern Physics*, 82, 3121–3195. <https://doi.org/10.1103/RevModPhys.82.3121>
- Haiman, Z., Kocsis, B., & Menou, K. (2009). Identifying the electromagnetic counterparts of cosmological standard sirens. *Physical Review D*, 80, 043513. <https://doi.org/10.1103/PhysRevD.80.043513>
- Harrison, F. A., et al. (2013). The nuclear spectroscopic telescope array (nustar) high-energy x-ray mission. *The Astrophysical Journal*, 770(2), 103. <https://doi.org/10.1088/0004-637X/770/2/103>
- Hennawi, J. F., Strauss, M. A., Oguri, M., Inada, N., Richards, G. T., Pindor, B., Schneider, D. P., Becker, R. H., Gregg, M. D., Hall, P. B., Johnston, D. E., Fan, X., Burles, S., Schlegel, D. J., Gunn, J. E., Lupton, R. H., Bahcall, N. A., Brunner, R. J., & Brinkmann, J. (2006). Binary quasars in the sloan digital sky survey: Evidence for excess clustering on small scales. *The Astronomical Journal*, 131, 1–23. <https://doi.org/10.1086/497989>

- Hoffman, L., & Loeb, A. (2007). Dynamics of triple black hole systems in hierarchical galaxy mergers. *Monthly Notices of the Royal Astronomical Society*, 377, 957–976. <https://doi.org/10.1111/j.1365-2966.2007.11694.x>
- Khan, F. M., Holley-Bockelmann, K., Berczik, P., & Just, A. (2013). Mergers of unequal-mass galaxies: Supermassive black hole binary evolution and structure of merger remnants. *The Astrophysical Journal*, 773, 100. <https://doi.org/10.1088/0004-637X/773/2/100>
- Khan, F. M., Preto, M., Berczik, P., Berentzen, I., Just, A., & Spurzem, R. (2012). Formation and hardening of supermassive black hole binaries in minor mergers of disk galaxies. *The Astrophysical Journal*, 749, 147. <https://doi.org/10.1088/0004-637X/749/2/147>
- Komossa, S., et al. (2003). Discovery of a binary agn in the ultraluminous infrared galaxy ngc 6240 using chandra [Available at arXiv:astro-ph/0212099]. *Astrophysical Journal Letters*.
- Kormendy, J., & Ho, L. C. (2013). *Coevolution (or not) of supermassive black holes and host galaxies* (Vol. 51). Annual Review of Astronomy; Astrophysics. <https://doi.org/10.1146/annurev-astro-082708-101811>
- Koss, M., Mushotzky, R., Treister, E., Veilleux, S., Vasudevan, R., & Trippe, M. (2012). Understanding dual active galactic nucleus activation in the nearby universe. *The Astrophysical Journal*, 746, L22. <https://doi.org/10.1088/2041-8205/746/2/L22>
- Koss, M. J., et al. (2017). A population of luminous accreting black holes with hidden mergers. *Nature Astronomy*, 1, 679–689. <https://doi.org/10.1038/s41550-017-0256-4>
- Lehmer, B. D., Basu-Zych, A. R., Mineo, S., Brandt, W. N., Eufrasio, R. T., Fragos, T., Hornschemeier, A. E., Luo, B., Xue, Y. Q., Bauer, F. E., Gilfanov, M., Ranalli, P., Schneider, D. P., Shemmer, O., Tozzi, P., Trump, J. R., Vignali, C., Wang, J.-X., Yukita, M., & Zezas, A. (2016). The evolution of normal galaxy x-ray emission through cosmic history: Constraints from the 6 ms chandra deep field-south. *The Astrophysical Journal*, 825, 7. <https://doi.org/10.3847/0004-637X/825/1/7>
- Liu, X., Greene, J. E., Shen, Y., & Strauss, M. A. (2010). Cosmological evolution of supermassive black holes. ii. evidence for downsizing of spin evolution. *The Astrophysical Journal*, 715, L30–L34. <https://doi.org/10.1088/2041-8205/715/1/L30>

- Lousto, C. O., & Zlochower, Y. (2012). Gravitational recoil from accretion-aligned black hole binaries. *Physical Review Letters*, 108, 231102. <https://doi.org/10.1103/PhysRevLett.108.231102>
- Lusso, E., Hennawi, J. F., Comastri, A., Zamorani, G., Richards, G. T., Vignali, C., Treister, E., Schawinski, K., Salvato, M., & Gilli, R. (2018). The close agn reference survey (cars): Mrk 1018 returns to the shadows after 30 years as a seyfert 1. *Astronomy Astrophysics*, 617, A121. <https://doi.org/10.1051/0004-6361/201833520>
- Mayer, L., Kazantzidis, S., Escala, A., & Callegari, S. (2010). Direct formation of supermassive black holes via multi-scale gas inflows in galaxy mergers. *Nature*, 466, 1082–1084. <https://doi.org/10.1038/nature09294>
- Mayer, L., Kazantzidis, S., Madau, P., Colpi, M., Quinn, T., & Wadsley, J. (2007). Rapid formation of supermassive black hole binaries in galaxy mergers with gas. *Science*, 316, 1874–1877. <https://doi.org/10.1126/science.1141858>
- Merloni, A., Predehl, P., Becker, W., Böhringer, H., Boller, T., Brunner, H., Brusa, M., Dennerl, K., Freyberg, M., Friedrich, P., Hasinger, G., Meidinger, N., Mohr, J. J., Nandra, K., Rau, A., Reiprich, T. H., Robrade, J., Salvato, M., Santangelo, A., ... Zimmermann, H.-U. (2012). Erosita science book: Mapping the structure of the energetic universe. *arXiv:1209.3114*.
- Merritt, D., & Milosavljević, M. (2005). Massive black hole binary evolution. *Living Reviews in Relativity*, 8, 8. <https://doi.org/10.12942/lrr-2005-8>
- Milosavljević, M., & Merritt, D. (2001). Formation of galactic nuclei. *The Astrophysical Journal*, 563, 34–62. <https://doi.org/10.1086/323830>
- Myers, A. D., Richards, G. T., Brunner, R. J., Schneider, D. P., Strand, N. E., Hall, P. B., Blomquist, J. A., & York, D. G. (2008). Observational evidence for agn feedback in early-type galaxies. *The Astrophysical Journal*, 678, 635–667. <https://doi.org/10.1086/529576>
- Nandra, K., Barret, D., Barcons, X., Fabian, A., den Herder, J.-W., Piro, L., Watson, M., Adami, C., Aird, J., Afonso, J. M., Alexander, D., Argiroffi, C., Amati, L., Arnaud, M., Atteia, J.-L., Audard, M., Badenes, C., Ballet, J., Bally, J., ... Vito, F. (2013). The hot and energetic universe: A white paper presenting the science theme motivating the athena+ mission. *arXiv:1306.2307*.

- Nyland, K., Young, L. M., Wrobel, J. M., Sarzi, M., Morganti, R., Alatalo, K., Blitz, L., Bournaud, F., Bureau, M., Cappellari, M., Crocker, A. F., Davies, R. L., Davis, T. A., de Zeeuw, P. T., Duc, P.-A., Emsellem, E., Khochfar, S., Krajnović, D., Kuntschner, H., ... Young, J. (2018). The next generation virgo cluster survey (ngvs). xxx. the environments of nucleated galaxies in the virgo cluster and in the field. *The Astrophysical Journal*, 859, 144. <https://doi.org/10.3847/1538-4357/aabfed>
- Preto, M., Berentzen, I., Berczik, P., & Spurzem, R. (2011). Fast coalescence of massive black hole binaries from mergers of galactic nuclei: Implications for low-frequency gravitational-wave astrophysics. *The Astrophysical Journal Letters*, 732, L26. <https://doi.org/10.1088/2041-8205/732/2/L26>
- Rieke, G. H., Wright, G. S., Böker, T., Bouwman, J., Colina, L., Glasse, A., Gordon, K. D., Greene, T. P., Guedel, M., Henning, T., Justtanont, K., Lagage, P.-O., Meixner, M. E., Nørgaard-Nielsen, H. U., Ray, T. P., Ressler, M. E., van Dishoeck, E. F., & Waelkens, C. (2015). The mid-infrared instrument for the james webb space telescope, i: Introduction. *Publications of the Astronomical Society of the Pacific*, 127, 584. <https://doi.org/10.1086/682252>
- Roming, P. W. A., et al. (2005). The swift ultra-violet/optical telescope. *Space Science Reviews*, 120, 95–142. <https://doi.org/10.1007/s11214-005-5095-4>
- Rosa, A., et al. (2022). Optically selected dual agn study in x-ray. *Monthly Notices of the Royal Astronomical Society*, 519(4), 5149–5160. <https://doi.org/10.1093/mnras/stac3664>
- Ryu, T., Perna, R., Haiman, Z., Ostriker, J. P., & Stone, N. C. (2018). On the gravitational wave background from black hole binaries after the first ligo detections. *The Astrophysical Journal*, 854, L8. <https://doi.org/10.3847/2041-8213/aaad0e>
- Satyapal, S., Secrest, N. J., McAlpine, W., Ellison, S. L., Fischer, J., & Rosenberg, J. L. (2014). Revealing hidden dual agn with chandra: Hints from the optical. *The Astrophysical Journal*, 784, 113. <https://doi.org/10.1088/0004-637X/784/2/113>
- Shen, Y., Hwang, H.-C., Zakamska, N., & Liu, X. (2019). Varstrometry for off-nucleus and dual sub-kpc agn (vodka): How well centered are low-z agn? *The Astrophysical Journal Letters*, 885(1), L4. <https://doi.org/10.3847/2041-8213/ab4b54>

- Treister, E., Schawinski, K., Urry, C. M., & Simmons, B. D. (2012). Major galaxy mergers and the growth of supermassive black holes in quasars. *The Astrophysical Journal*, 758, 39. <https://doi.org/10.1088/0004-637X/758/1/39>
- Urry, C. M., & Padovani, P. (1995). Unified schemes for radio-loud active galactic nuclei. *Publications of the Astronomical Society of the Pacific*, 107, 803. <https://doi.org/10.1086/133630>
- Weston, M. E., McIntosh, D. H., Brodwin, M., Mann, J., Cooper, A., McConnell, A., & Nielsen, J. L. (2017). Spitzer observations of long-term infrared variability among young stellar objects in chamaeleon i. *The Astrophysical Journal*, 838, 149. <https://doi.org/10.3847/1538-4357/aa6620>
- Xmm-newton users handbook*. (2021). ESA/XMM-Newton. https://xmm-tools.cosmos.esa.int/external/xmm_user_support/documentation/uhb/XMM_UHB.pdf
- Yu, Q. (2002). Evolution of massive binary black holes. *Monthly Notices of the Royal Astronomical Society*, 331, 935–958. <https://doi.org/10.1046/j.1365-8711.2002.05242.x>
- Yu, Q., & Tremaine, S. (2003). The eccentricity distribution of coalescing black hole binaries driven by the kozai mechanism in globular clusters. *The Astrophysical Journal*, 599(2), 1129–1138. <https://doi.org/10.1086/379546>